INVESTIGATION OF HALF-QUANTIZED FLUXOID STATES IN Sr_2RuO_4 MESOSCOPIC SUPERCONDUCTING RINGS

BY

JOONHO JANG

DISSERTATION

Submitted in partial fulfillment of the requirements
for the degree of Doctor of Philosophy in Physics
in the Graduate College of the
University of Illinois at Urbana-Champaign, 2012

Urbana, Illinois

Doctoral Committee:

Professor Dale J. Van Harlingen, Chair
Associate Professor Raffi Budakian, Director of Research
Professor Eduardo Fradkin
Professor William P. King

Abstract

Spin-triplet superconductors can support exotic objects, such as chiral edge currents and half-quantum vortices (HQVs) characterized by the nontrivial winding of the spin structure. In this dissertation, we present cantilever magnetometry measurements performed on mesoscopic samples of Sr_2RuO_4, a spin-triplet superconductor.

Satisfying the total anti-symmetric property of the Cooper pair wave function, Sr_2RuO_4 is theoretically suggested to have angular momentum $L=1$ and form domain structure with $p_x \pm ip_y$ order parameter that corresponds to $L_z = \pm 1$. For micron-size samples, only a few number of domains would exist and signatures of domain walls and edge currents are expected to be measurable with current sensitivity. From the measurements of fluctuations of magnetic signal and the signatures of vortex entries, we found no evidence to support broken time-reversal symmetry (TRS) in these crystals. We argue that various scenarios exist to explain the negative result while still assuming the TRS breaking chiral order parameter.

Also, micron-size annular-shaped Sr_2RuO_4 crystals were used to observe transitions between fluxoid states. Our observation of half-integer transitions is consistent with the existence of HQVs in a spin-triplet superconductor. Stability of the half states with an in-plane magnetic field is explained by the spin polarization in consequence of a differential phase winding of up and down spin components. These spin and charge dynamics can also be revealed in the current response to phase winding across a weak-link junction. The junctions were fabricated within ring geometry. The phase is varied by the external magnetic field and the current is calculated by measuring the magnetic moments of the ring. The current response shows second harmonics when the in-plane magnetic field is applied, and the data are successfully fitted when Gibbs free energy is expressed with additional spin degree of freedom.

Our observations are consistent with spin-triplet pairing of the Sr_2RuO_4, while requiring more investigations to confirm $p_x \pm ip_y$ order parameter in the crystal.

To my parents and Chang Joo

Acknowledgement

I want to thank my advisor Prof. Raffi Budakian for being an outstanding teacher and researcher. It has been a challenge to build everything in the lab from scratch, but it ended up being a great joy to observe what we finally accomplished. He was always enthusiastic and available when I need help. I also would like to thank all the group members for making our lab such comfortable and pleasant. I can't imagine a better work and research environment. I would like to thank John Nichol, Xu Wang, Tyler Naibert, Gregory Polshyn, Karthik Jambunathan, Fei Tan and Xin Zhao for their friendship, conversation, and assistance whenever I needed them.

My thanks also go to theorists I have pleasantly worked with. I had numerous discussions with Prof. Paul Goldbart, David Ferguson, Victor Vakaryuk and Suk Bum Chung. They have been an amazing collaborator and his attentiveness and engagement at all stages of our work were invaluable. I also would like to thank Prof. Yoshi Maeno and his group at Kyoto University in Japan. Prof. Maeno and his crystal growing team played an essential role in the success of this research projects by providing me with the best Sr_2RuO_4 samples in the world.

The love of my family and friends has been a constant source of strength for me, and I want to thank my parents and Chang Joo for providing me with so much support. I cannot miss to mention the friendships with Hyungjoon Kim, Hyeongjin Ma, Young Il Joe, Jaseung Ku, Mao-Chuang Yeh Hyunk Shin Kwon, Won Seok Shin, and Lucas Urban, which made my time in Urbana and US much more colorful.

The work at the University of Illinois at Urbana-Champaign was supported by the U.S. Department of Energy Office of Basic Sciences, grant DEFG02-07ER46453 through the Frederick Seitz Materials Research Laboratory.

The work at Kyoto University was supported by the grants-in-aid for the Global Centers of Excellence “Next Generation of Physics” programs from the Ministry of Education, Culture, Sports, Science and Technology of Japan. I also acknowledge partial support from Samsung Scholarship Foundation.

Table of content

Chapter 1

Introduction

Superconductivity is the phenomenon characterized by the loss of electrical resistance and the appearance of perfect diamagnetism below critical temperature. Due to its immense industrial applications and influence to fundamental science, the research of superconductivity became the one of the most prolific topic in physics since its discovery almost a century ago.

The electrical resistance of metallic conductors decreases by lowering temperature and reaches a finite value near zero temperature. However, that of a superconductor suddenly drops to absolute zero at T_c, transition temperature, suggesting a phase transition. To explain it, one needs to employ quantum mechanics and account for many-body effects. At large, there were two successful attempts to describe the phenomenon, which are Ginzburg-Landau theory [1] and BCS (Bardeen-Cooper-Schrieffer) theory [2].

The Ginzburg-Landau theory describes the emergent superconducting phase with a free energy functional of an order parameter representing the density of the phase, therefore nonzero only in the superconducting state. By minimizing the free energy via variational principle, Ginzburg-Landau equations are derived and the solutions give the spatial variation of the superconducting density and current. The parameters of the equation includes the penetration depth λ, a length scale that magnetic fields penetrate into a superconductor, and the coherence length ξ, a length scale the superconducting order parameter varies, and those are expressed by material specific values such as effective mass. One advantage of the theory is that it is phenomenological not depending on any particular microscopic model, so that it can be applied to materials such as the high T_c cuprate superconductors where the microscopic mechanism of superconductivity is not clearly understood.

On the other hand, BCS theory is fully based on microscopic realism. Its basic element is the Cooper pair, which two electrons with opposite wave vector form with an arbitrarily small attractive interaction. These pairs of electrons in the ground state are separated from the excitations, quasi particles, by an energy gap Δ. The many-particle condensate wave function maintains phase coherence over macroscopic distances. Later, Gor'kov demonstrated that the Ginzburg-Landau theory is indeed a limit of the BCS theory close to the transition temperature and that the order parameter is directly proportional to the energy gap [3].

In most superconductors including element metals, the attraction between electrons is indirect via electron-phonons interactions. This interaction generates excessive positive charges around an electron to attract the other electron in the pair. The attraction is isotropic that the usual Cooper pairs form with its angular momentum with zero (s-wave pairing). The situation is quite different in more complex compounds superconductors, such as the heavy fermions, the organic superconductors, the borocarbides, the ruthenates and most notably the high T_c cuprate. While the exact mechanism of the attractive interaction is still debatable, many suspect it to be either antiferromagnetic or ferromagnetic spin fluctuations which favor anisotropic pairing mechanism. These categories of superconductors are more complicated than what the early developers of BCS theory initially conjectured and are called *unconventional* superconductors. Most of them have some finite angular momentum L of the pair wave function due to the anisotropic nature of the pair interaction. Moreover, to satisfy the overall anti-symmetric properties under particle exchange, odd L states need to be spin-triplet and even L to be spin-singlet. The famous high-T_c cuprate superconductors are believed to have L =2 state (d-wave).

Superconductors are not the only example where Cooper pairing happens: superfluid ^{3}He has been theoretically and experimentally verified to be the rare instance to form spin-triplet p-wave pairing. It exhibited many exciting features including topological excitations. However, triplet paring in a superconductor is rare.Sr_2RuO_4 is one of only few known superconductors thought to exhibit triplet pairing with transition temperature of 1.5 K [4], and is believed superconducting version of the superfluid of ^{3}He.

In this paper we focus the superconducting properties of Sr_2RuO_4, especially the order parameter and topological excitations in analogy to the He-3 superfluid. In Chapter 2 we will present a summary of the properties of Sr_2RuO_4 and theoretical background of the experiments we performed. Chapter 3 contains technical details about sample preparation and measurement instruments. In Chapter 4 we describe experiments to determine an existence of chiral domain and edge current. Chapter 5 is regarding to the observation of half-height magnetization steps and half-quantized fluxoid states in a mesoscopic rings. Chapter 6 contains experimental details about weak-link fabrication and current-phase relationship measurements.

Chapter 2

Superconducting properties of Sr_2RuO_4

Sr_2RuO_4 has a body centered tetragonal crystal structure of the type K_2NiF_4 type perovskite polymorph [4]. In contrast to most materials with the same crystal structure, it exhibits little structural distortion, and thus no phase transition to a different crystalline structure at low temperature. The material was the first layered oxide superconductor found without copper, with a fairly low transition temperature of 1.5 K. A large number of research activity were performed trying to understand the superconductivity in this material partly because it is a normal Fermi-liquid, while has a same structure to a high T_c superconductor, $La_{2-x}Ba_xCuO_4$ (see Figure 2.1). It presents a good opportunity to investigate unconventional superconductivity based on a well understood normal state. Thin films could not be made to be superconducting with high transition temperature due to disorders and surface scatterings, even though it was able to grown up to 10 cm size single crystals of very high purity. For those who are interested in more detail, a thorough review on the superconducting properties of Sr_2RuO_4 is also given by one of the collaborators of our research [5].

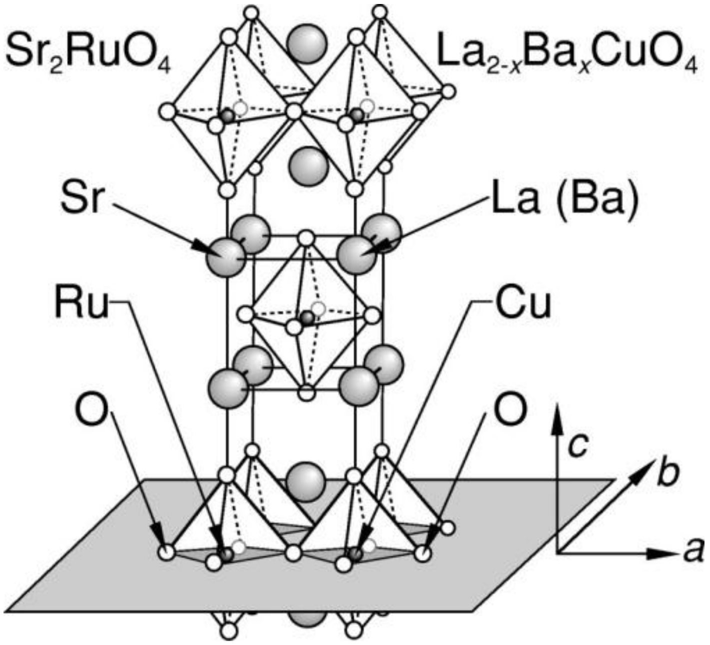

Figure 2.1 The layered perovskite structure common to ruthenate and cuprate superconductors. From [5].

2.1. Properties of normal state

The successful growth of exceptionally high purity single crystals of Sr_2RuO_4 enabled the measurement of quantum oscillations, such as Shubnikov-de Haas and de Haas-van Alphen effects [6]. Very long mean free path and relatively low critical magnetic field of this material happened to be crucial for the success of the quantum oscillation measurement since these oscillations decay rapidly with more scattering and increasing temperature. Critical information about the electronic structure of the material can be extracted with the measurements; the measurement was used to confirm the structure of the rather complicated Fermi surface. The measured Fermi surface is shown in Figure 2.2. The Fermi surface sheets are cylindrical and has three disconnected Fermi sheet that were labeled α, β and γ. The β and γ are electron-like, and the α has hole-like properties [7,8].

Interestingly, charge density wave (CDW) phase is observed in this material around 30K. It is attributed to the Fermi surface nesting, and relation to superconducting state is relatively unknown. Electronic specific heat measured at low temperature is considerably larger than calculated value. Together with the CDW phase it suggests strong correlation effect and explains the failure of the local density approximation [7]. Otherwise, the low temperature properties of the crystal are well explained by a two-dimensional Fermi-liquid picture. Indeed, the electrical resistivity is highly anisotropic, and the ratio of the in-plane to the c-axis resistivity varies about an order of magnitude. However, both resistivities have same T^2 temperature dependence below about 20 K, and thus their ratio doesn't change much. At room temperature, the c-axis resistivity first increases when cooling, reaches a maximum at about 130 K, and then decreases. That non-monotonic temperature dependence is coming from a transition from incoherent transport along the c-axis (due to high anisotropy of the crystal structure) at high temperature to a full 3d transport in the crystal at lower temperature. A low residual resistivity of ~0.4 $\mu\Omega$-cm is attained and corresponding ideal superconducting transition temperature approaching ~1.5K indicates very high purity in the crystal (see section 2.2.1). The static magnetic susceptibility is close to isotropic, a sign that it is not dominated by an anisotropic electron structure but instead by the spin or Pauli term. Nuclear magnetic resonance studies of ^{17}O and ^{101}Ru sites give evidence for ferromagnetic fluctuations [9], and inelastic neutron scattering measurements [10] show consistent results with a theoretical prediction of incommensurate spin fluctuations, giving some hint of the superconducting paring mechanism.

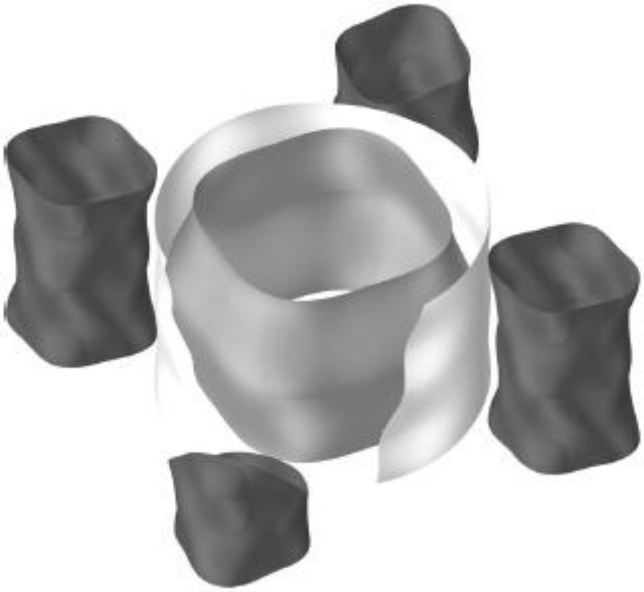

Figure 2.2 The experimentally constrained Fermi surface of Sr_2RuO_4. The hole-like α sheet is shown by the four dark cylinders. The β sheet is the central cylinder with a nearly square cross section. The γ sheet is the outer central cylinder with a nearly circular cross section. From [8].

2.2. Superconducting state properties

2.2.1. Effect of impurities and Ginzburg-Landau parameters

Maeno and collaborators in Kyoto University in Japan measured the dependence of T_c on the oxygen partial pressure during high temperature annealing [11]. It showed insensitivity of T_c on the annealing conditions, unlike in cuprates, and thus established experimental evidence of exceptional chemical stability of this material. It came as a surprise because the superconductivity in Sr_2RuO_4 was expected to show some similarities to the cuprates due to their similar crystal structures.

Studies on the non-magnetic impurity effect on T_c of the superconductivity together with the absence of the coherence peak, known as Hebel-Slichter peak, in

^{101}Ru NMR and Nuclear Quadrupole Resonance (NQR) experiments, suggested the unconventional character in superconductivity of Sr_2RuO_4. When a large variation in the transition temperatures of different batches was observed in experiments, with the fact that the oxygen annealing experiment showed that doping doesn't change superconducting property effectively, a plausible explanation was the presence of impurities. According to Anderson's theorem, magnetic impurities suppress superconductivity because they act as Cooper pair breakers while elastic scattering of Cooper pairs due to non-magnetic impurities does not diminish the energy gap of conventional superconductors [12]. The non-magnetic scattering effectively averages the Fermi wave vectors of the pairs because time-reversal pairs under the impurity potential still from Cooper pairs with same gap potential. Thus, for a gap isotropic in phase, the gap maintains finite value after the averaging, and it does not destroy superconducting gap. For unconventional superconducting gap symmetries that exhibit sign changes, the averaging of the order parameter over the Fermi surface become zero, and hence the gap will be suppressed by non-magnetic impurities if the scattering length is comparable to the superconducting coherence length ξ. A nice experimental demonstration of the phenomenon was done on Sr_2RuO_4. Mackenzie et al. measured the density of impurities in crystals with varying transition temperatures [13]. A microprobe analysis was used to measure density of elements with atomic numbers between 11 and 83 with a precision better than 50 ppm. With correlations between traces of silicon and aluminum, the residual resistivity of the samples, and their transition temperatures, it gave a clear indication that superconductivity in Sr_2RuO_4 is destroyed by non-magnetic impurity scattering, thus providing evidence to unconventional superconductivity in this crystal. This suggested that the low T_c samples are contaminated with impurities and its superconducting properties might be also compromised. Also, it gave an important guide line to use residual resistivity for determining the purity of a sample. Samples with mean free paths as long as 3 μm have been synthesized achieving a transition temperature of ~1.5 K, which is theoretical maximum by fitting curves of impurity vs T_c. A following study showed that the same pair breaking effect by impurities could be also achieved when crystal defects are formed through changes to growth conditions [14]. All these series of experiments supports the theoretical suggestion that Sr_2RuO_4 is an unconventional superconductor with additional symmetry breaking.

The Ginzburg-Landau parameters of the superconducting state was also measured by Maeno group [11,15]. They measured the in-plane and out-of-plane resistivity in applied magnetic fields on the crystals with transition temperatures ranging from 0.2 K to 1.49 K. Then they deduced values for the in-plane and out-of-plane critical field of $\mu_0 H_{c2\|ab}(0) = 1.5\,\mathrm{T}$ and $\mu_0 H_{c2\|c}(0) = 0.075\,\mathrm{T}$ by extrapolating the measured H_{c2} to zero temperature. Using the anisotropic Ginzburg-Landau formula, the coherence lengths of $\xi_{ab}(0) = 66\,nm$ and $\xi_c(0) = 3.3\,nm$ with an anisotropy $\xi_{ab}(0)\,/\,\xi_c(0) =$ 20 were obtained. To determine the Ginzburg-Landau parameter, they measured the low temperature specific heat and extracted from it the thermodynamic critical field $H_c(0) = 0.023\mathrm{T}$ [11]. The Ginzburg-Landau parameters were deduced to be $\kappa_{ab}(0) = 2.3$ and $\kappa_c(0) = 46$, which give penetration depths values of $\lambda_{ab}(0) = 152\,nm$ and $\lambda_c(0) = 3000 nm$.

2.2.2. Experiments on unconventional superconductivity

At superconducting transition, normal electrons form a superconducting condensate, consisting of Cooper pairs, and like other phase transitions a part of symmetry is spontaneously broken. The angular momentum of the relative motion of the constituent electrons in the pair becomes an important factor to categorize superconductivity. In conventional superconductors, only gauge symmetry is broken at the transition. The superconducting order parameter is a complex number and the Cooper pair orbital angular momentum is $L=0$. Under certain conditions the pairs form a more complicated structure and the angular momentum has non-zero value. The so-called unconventional superconductors break additional symmetries, such as the point group of the crystal lattice symmetry, the spin rotation symmetry, and the time-reversal symmetry (TRS). Thus, the superconducting order parameter symmetry becomes a subgroup of the symmetry group of the normal state. Group theory is a very useful tool to enumerate a list of allowed order parameter based on the crystal structure of the superconductor [16]. Order parameters consistent with experimental results are considered, and free energies of the order parameters are compared to give the energetically most favorable choice. Because the electrons satisfy Fermi statistics, even orbital angular momentum states correspond to an anti-symmetric spin-singlet pairing of the spins, while odd orbital pairing corresponds to symmetric spin-triplet pairing. Thus, spin-singlet pairing states come with orbital symmetries of s ($L=0$) and d ($L=2$) wave, etc., while spin-triplet pairings are accompanied with p ($L=1$), f ($L=3$), etc. It should be noted that in the presence of spin-orbit coupling and crystal fields the spin and angular momentum is not a good quantum number of the Hamiltonian; however, the notation is still valid with a good approximation in the case of Sr_2RuO_4, where the lattice and spin-orbit effects are sufficiently weak. Within a same irreducible representation (same L state), the additional symmetries can be broken, and it categorizes the phases. For example, a state with broken time-reversal symmetry can be represented by multicomponent complex order parameters transitioned from a real order parameter spin-triplet condensate by another phase transition. Transition temperatures of different phases in an irreducible representation are same [17].

There are a number of probes to distinguish the different order parameters by measuring the change in corresponding physical properties. First of all, the phase sensitive techniques directly measure the macroscopic order parameter symmetry using the Josephson effect. The anisotropy and polarity of the phase of the order parameter can be measured. Josephson interferometry and Scanning SQUID Microscopy successfully verified d-wave pairing symmetry of high-T_c superconductors. On the other hand, multiple phase transition can be detected. If observed, it differentiates other pairing symmetries from s-wave paring. They are usually observed by singularities in derivatives of the free energy. For example, the specific heat will have an additional peak at the transitions. By definition the additional phase transition indicates unconventional superconducting order in the material. Moreover, there are experiments that measure the electronic spin susceptibility of the material to distinguish spin singlet from spin triplet pairing. In singlet superconductors the susceptibility goes to zero according to Yoshida function below superconducting transition because the opposite spin pairing of Cooper pairs diminishes the ability of conduction electrons to be polarized under the influence of the external magnetic fields, while in triplet superconductors it can remain finite even at zero temperature. As an example, the Knight shift measures the shift in NMR frequency caused by the electronic spin susceptibility in the conduction band via hyperfine interaction. The other type of experiments includes measurements of average energy gap over the Fermi surface. The average becomes zero if the order parameter change sign under inversion. Examples include the sensitivity of superconductivity to non-magnetic impurities and the presence of a coherence peak of NMR relaxation rate near the transition. Lastly, detecting the nodal structure in the gap function can confirm the unconventionality in the superconducting symmetry. The temperature dependence of the specific heat, penetration depth, and NMR relaxation rate is exponential for s-wave conventional superconductors. The presence of the nodes is reflected on the density of states due to energy gap closing, especially at low temperatures, and the temperature dependence becomes power-law in the presence of nodes. For example, T^2 are expected for line nodes and T^3 for point nodes, which reflect the residual density of state near zero temperature. Some of these techniques have been improved giving directional information of the nodes, such as thermal conduction and specific heat in magnetic field, and ultrasound attenuation.

Recently significant and interesting types of experiments include measurements that probe broken TRS and exotic vortices. Muon Spin Relaxation (μSR) measured an internal spontaneous magnetic moment below T_c [18]; the high resolution polar Kerr effect measured an antisymmetric component of the real and imaginary parts of the dielectric tensor [19]; and scanning SQUID microscopy probes magnetic fields generated by the TRS broken current [20]. In Chapter 4, cantilever magnetometry of the TRS chiral current in a micron size sample will be presented. Additionally, the exotic vortices realized by the existence of multiple order parameters were theoretically predicted and partially observed in ^{3}He superfluid. Thus, our measurement of half-quantized fluxiod states, a generalized half-quantum vortex, will be a significant addition for elucidating unconventional superconductivity in Sr_2RuO_4. However, the interpretation of these experiments should be careful. It takes many consistent measurements with same conclusions before the actual order parameter can be confirmed.

2.2.3. Spin triplet superconductivity in Sr_2RuO_4

Order parameters in spin triplet superconductors are expressed in terms of the gap matrix $\Delta(\mathbf{k})$ that can be written as a 2 x 2 matrix in the form [5]

$$\Delta(\mathbf{k}) = \begin{pmatrix} \Delta_{\uparrow\uparrow} & \Delta_{\uparrow\downarrow} \\ \Delta_{\downarrow\uparrow} & \Delta_{\downarrow\downarrow} \end{pmatrix}, \tag{2.1}$$

where $\mathbf{k}$ is a unit vector in a direction of wave vector and the elements are defined in a spin-space of paired electrons. In the triplet case, $\Delta_{\uparrow\downarrow} = \Delta_{\downarrow\uparrow} = \Delta_0$. The $\mathbf{d}$-vector formalism is another way to express the superconducting energy gap, used prolifically in literatures of ^{3}He superfluid. In the formalism the matrix is replaced by a three component complex vector $\mathbf{d}(\mathbf{k}) = [d_x(\mathbf{k}), d_y(\mathbf{k}), d_z(\mathbf{k})]$ with

$$\Delta(\mathbf{k}) = \begin{pmatrix} \Delta_{\uparrow\uparrow} & \Delta_0 \\ \Delta_0 & \Delta_{\downarrow\downarrow} \end{pmatrix} = \begin{pmatrix} d_x + id_y & d_z \\ d_z & d_x + id_y \end{pmatrix}. \tag{2.2}$$

It has an advantage of transforming as a vector under the rotation of spins as well as having a compact form analogous to the gap function of singlet superconductors.

The wave function of a triplet superconductor can be expressed as

$$|\psi> = \Delta_{\uparrow\uparrow} + \Delta_{\downarrow\downarrow} + \Delta_0(|\uparrow\downarrow>), \tag{2.3}$$

where the bases $|\uparrow\uparrow>$, $|\downarrow\downarrow>$ and $(1/\sqrt{2})(|\uparrow\downarrow> + |\downarrow\uparrow>)$ correspond to the spin basis vectors of $S_z = 1$, -1 and 0, respectively. If the coordinates are changed to x, y and z defined as

$$\mathbf{x} = |S_x = 0> = \frac{1}{\sqrt{2}}(-|\uparrow\uparrow> + |\downarrow\downarrow>),$$

$$\mathbf{y} = |S_y = 0> = \frac{1}{\sqrt{2}}(|\uparrow\uparrow> + |\downarrow\downarrow>), \tag{2.4}$$

$$\mathbf{z} = |S_z = 0> = \frac{1}{\sqrt{2}}(-|\uparrow\downarrow> + |\downarrow\uparrow>),$$

then the state is written as

$$|\psi> = \sqrt{2}(d_x\mathbf{x} + d_y\mathbf{y} + d_z\mathbf{z}). \tag{2.5}$$

The quasiparticle excitation energy spectrum then will be given by

$$E_k = \sqrt{\epsilon_k^2 + \mathbf{d}\,\mathbf{d}^* \pm |\mathbf{d} \times \mathbf{d}^*|}, \tag{2.6}$$

,where E_k is the quasiparticle energy and ϵ_k is the excitation energy measured from the chemical potential.

For a unitary state with $\mathbf{d}\times\mathbf{d}^*=0$, $\mathbf{d}\mathbf{d}^*$ becomes the square of the energy gap $|\Delta(\mathbf{k})|^2$, and all the electrons are paired at zero temperature. The magnitude of the vector is proportional to the energy gap and the direction is normal to the plane in which the electrons are equal spin paired. On the other hand, non-unitary states have two distinct energy gaps. If one of them vanishes, finite density of quasiparticle can be observed at zero temperature. Non-unitary states break TRS and possibly have a net magnetic moment. Even if largely screened by the Meissner effect, a small fraction of the magnetization can survive at impurities or defects sites or at the edge of a crystal, where the order parameter is suppressed from the bulk one.

The measurement of the spin susceptibility in the superconducting state by NMR was the most compelling evidence for spin-triplet pairing in Sr_2RuO_4. The spin susceptibility in superconductors is dominated and masked by Meissner screening currents and need to be measured indirectly through experiments such as the Knight shift measurements. The NMR frequency shift of a nucleus reflects the spin susceptibility change of conduction electrons via the indirect hyperfine contact interaction between s-wave valence electrons and the nucleus. The signal is a combination of an orbital part due to Landau diamagnetism of the core electrons and Pauli paramagnetism due to a spin polarization of the conduction electrons. With spin-singlet pairing of electrons, the spin susceptibility should drop following Yoshida function below T_c [23]. However, with the equal-spin paired superconductors, the susceptibility will remain same as normal metal’s. Ishida et al. performed NMR knight shift measurements on ^{17}O and ^{101}Ru [21,22]. The absence of change in the spin susceptibility through the superconducting transition indicates the existence of an equal spin pairing direction and thus spin-triplet paring in the superconducting state.

The consistent conclusion was obtained with polarized neutron scattering that also measures the spin susceptibility [23]. An applied magnetic field induces a periodic magnetization density in the crystal, and refraction gives Fourier components at reciprocal lattice vectors. By carefully differentiating spatially-varying components of the magnetization, spin susceptibility can be measured, even in the superconducting state. They found the spin susceptibility doesn’t change when temperature varies through T_c ,an additional evidence to the spin-triplet paring. Additionally, the odd symmetry confirmed by the Josephson interferometry provides consistent evidence for spin triplet pairing in superconducting Sr_2RuO_4.

2.2.4. Chiral p-wave order parameter and its domains

Among the triplet order parameters allowed by symmetry, fully-gapped unitary p-wave order parameter is energetically favored [5]. The $\mathbf{z}(p_x \pm ip_y)$ order parameter was proposed in an analogy to the A-phase of superfluid ^{3}He [24]. It has complex order parameter which breaks TRS, and thus a spontaneous magnetization is expected to be observed below the transition temperature. In Chapter 4, we talk more about the properties associated with the order parameter.

In most cases, a spontaneous magnetization that appears below T_c is expected for the order parameter with broken TRS. Due to screening current, only suppressed magnetization is observable on length scales smaller than penetration depth, or at defects where the screening is weak. Luke et al. used spin-polarized muons to penetrate into the inside of a sample and interact with the local magnetic environments. They measured a directional tendency of positron emission of the muon decay, which contains information about the local magnetic fields [18]. The study shows spontaneous magnetization at T_c with an exponential distribution of the relaxation rate, which is interpreted as an indication of a broad distribution of magnetic fields from a dilute distribution of current sources. They measured samples of various T_c and found that the spontaneous magnetization always coincided with the superconductivity to rule out a magnetic phase accidentally happened to be at the superconducting transition temperature. It was concluded that the increased relaxation rate was caused by broken TRS. An additional piece of evidence for the TRS broken order parameter came from a small angle neutron scattering experiment [25]. It showed that vortices form a square lattice, neither triangular nor hexagonal, in SRO at all field-temperature phase space. This is consistent with a TRS-breaking chiral state, which requires two components in order parameter.

Interestingly, two Stanford groups reported experimental result which is not consistent with each other. Xia et al. performed a measurement of the polar Kerr effect on the surface of Sr_2RuO_4 crystal [19] and measured the rotation of polarization angle caused by the existence of an antisymmetric component to the frequency dependent dielectric tensor, suggesting broken TRS. They found a polar Kerr effect that appears at T_c and whose magnitude increases as the temperature is lowered. On the other hand, Kirtley et al. [20] used SQUID microscopy with a spatial resolution of ~8 μm to image domain and surface currents generated by the order parameter domains. They argued that the magnitude of the current is not large enough to support the existence of domains larger than ~2 μm. There are a few proposals to resolve this inconsistency, and this issue will be revisited in Chapter 4.

The spin-triplet chiral order parameter is represented by the $\mathbf{d}$-vector [5]

$$\mathbf{d} = \Delta_0 \mathbf{z}(k_x \pm ik_y) = \Delta_0 \begin{pmatrix} 0 \\ 0 \\ k_x \pm ik_y \end{pmatrix} \tag{2.7}$$

Because the direction of the $\mathbf{d}$-vector defines the spin wave function, $\mathbf{d} \| \mathbf{z}$ leads to an equally weighted superposition of |↑↑> and |↓↓> states for a quantization axis within the plane. This is the two-dimensional version of the A-phase of superfluid ^{3}He with an orbital angular momentum L = 1. In the presence of crystal fields, the directions of the spin wave function lock on the axes of the crystal. Thus the $\mathbf{d}$-vector can be expressed in terms of spherical harmonics as

$$Y_{1\pm1} = \left(\frac{3}{8}\pi\right)^{1/2} \sin\theta \exp(\pm i\phi) = \left(\frac{3}{8}\pi\right)^{1/2} (k_x \pm ik_y). \tag{2.8}$$

with $L_z = \pm 1$. The non-zero angular momentum represents the Cooper pairs' relative orbital motion in the xy-plane with either clockwise or counterclockwise rotation and leads to broken TRS.

The order parameter domains are formed as a consequence of the complicated dynamics of the chiral state with broken time-reversal symmetry. Volovik et al. have classified states with broken TRS with non-zero internal angular momentum of Cooper pairs as ferromagnetic states that, in the ground state, a current should flow along the surface of the material [26,27]. The order parameter of Sr_2RuO_4 has finite orbital angular momentum proportional to the number of Cooper pairs in the condensate [28]. To self-consistently include the Meissner effect, a screening current will flow within a length scale of penetration depth to cancel the field generated by the ferromagnetic current throughout the bulk of the material. As a consequence, magnetization inside the bulk is strongly suppressed, but there will still be a magnetic moment at the surfaces as well as at sites with a suppressed superconducting order parameter (i.e. defects and impurities). Order parameter domains also can form due to the discrete symmetry and degeneracy of the order parameter. The domains are called chiral domains and the two degenerated chirality is represented by order parameters either $p_x + ip_y$ or $p_x - ip_y$. In some way this is similar to those in ferromagnetic materials. However, domain formation in the superconducting order parameter costs the domain wall energy while the ferromagferromagnetic domain formation saves energy by dipole interaction [27,29]. It is believed that they will easily get pinned at defects or impurities sites because the domain walls are energetically costly; however, there is no clear observation up to now. Sigrist et al. have performed several numerical calculations on chiral domains: they directly solved the Ginzburg-Landau equations and did the self-consistent semi-classical calculation to analyze the quasi-particle states to investigate complex superconductivity in low magnetic fields [30,31]. It was found that there are a spontaneous current in the wall and a counter-flowing screening current. Thus, a single domain superconductor with a singly connected geometry would have a finite net magnetization. Near the domain wall, because order parameter is a tensor, the normal component of the order parameter to the wall is suppressed while the one parallel is enhanced. Thus, it gives the two possibilities for the order parameter changes through the domain wall either by vanishing in the center of the wall or having a phase rotation with a finite modulus everywhere. It also was shown that mid-gap states in the local density of states are one of characteristics in the domain walls.

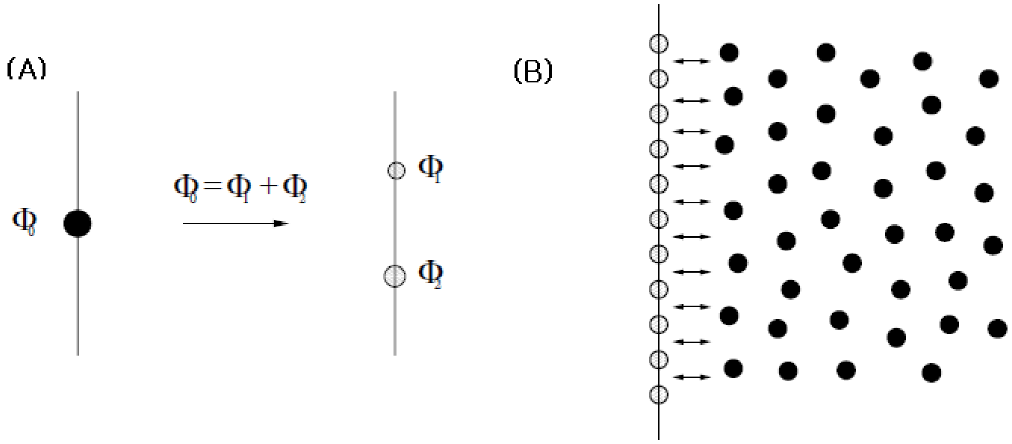

Figure 2.3 Vortices strongly pinned by a domain wall. Grey cirtcles are fractional vortices and dark ones are full vortices. (A) A full quantum vortex decays into two fractional vortices. (B) Fully occupied domain wall acts as a fence for the full vortices. From [35]

While so far there is no “smoking gun” evidence for the formation of domains, strong evidence is given indirectly by observing the vortex-domain wall interaction. The current flowing along the domain wall is strongly interacting with and vortices due to a Lorentz force. The rate of vortex creep dynamics was measured in three superconductors with broken time reversal symmetry: UPt_3, $U_{1-x}Th_xBe_{13}$ and Sr_2RuO_4 [32–34]. They found unusually high pinning effect in all three materials at low temperature. When observing the two heavy fermions UPt_3 and $U_{1-x}Th_xBe_{13}$ below the lower transition temperature and below 50mK in Sr_2RuO_4, the temperatures for which chiral order parameters are expected to from, the rate of vortex creep drops to nearly zero for several hours, and this may be due to a highly unusual pinning mechanism of the domain walls. This can be explained in terms of “fences” that prevent the vortices from moving around the superconductor [35]. It was found that a vortex with integer flux quantum can degenerate into two or more vortices with fractional flux on domain walls (see Figure 2.3). Thus, these vortices cannot easily move away from the wall, and they become very efficient pinning centers to vortex motion. These vortex dynamics at domain walls were pointed out as a possible mechanism of the ultrasound attenuation in UPt_3 [16] and vortex coalescence in Sr_2RuO_4 [36].

2.2.5. Half-quantum vortex

While known superconductors are characterized by the spin-singlet pairing of the electrons that constitute the superconducting flow, Sr_2RuO_4 (SRO) which, much like the A-phase of superfluid ^{3}He, might exist in the equal-spin pairing (ESP) phase [5]. This phase has been proposed to host half-quantum vortices (HQVs), which are characterized by the relative winding of the phase of the spin-up and spin-down components of the superfluid order parameter [37,38]. In addition to being of basic scientific interest, HQVs are expected to give rise to zero-energy Majorana quasiparticles [39,40], which have been suggested as a resource for topological quantum computation [41].

The ESP state may be thought of as comprising two weakly interacting condensates, having Cooper-pair spin configurations, $\left|\uparrow\uparrow\right\rangle$ and $\left|\downarrow\downarrow\right\rangle$, defined with respect to a common (i.e., ESP) axis. An HQV corresponds to the winding of the phase of only one of these condensates around a contour that encircles the HQV core, e.g., $(\Delta\theta_\uparrow, \Delta\theta_\downarrow) = (\pm 2\pi, 0)$ or $(0, \pm 2\pi)$, producing half of the magnetic moment of a conventional (i.e., full-quantum) vortex (FQV), for which $\Delta\theta_\uparrow = \Delta\theta_\downarrow = \pm 2\pi$. The Meissner response of the superconductor screens charge currents over the length-scale of the London penetration depth λ; however, any (charge-neutral) spin currents go unscreened. Consequently, the kinetic energy of an isolated HQV diverges logarithmically with the system size, whereas the kinetic energy of an FQV would remain finite. Hence, a single HQV may not be energetically stable in a macroscopic sample, whereas, according to [42], a single HQV could be stable in a mesoscopic SRO sample of size comparable to or smaller than λ.

For an ESP superconductor, the two condensates bring the two integer-valued winding numbers $n_\uparrow$ and $n_\downarrow$. Then, the role of *n* is played by the half-sum $n=(n_\uparrow+n_\downarrow)/2$. The integer-fluxoid (IF) state of the annulus—the coreless analog of the FQV state—corresponds to the common winding of the condensates (i.e., $n_\uparrow=n_\downarrow$), whereas the half-fluxoid (HF) state—the coreless analog of the HQV state—corresponds to winding numbers that differ by unity (i.e., $n_\uparrow=n_\downarrow\pm1$). Thus, equilibrium transitions between the IF and HF states would change *n* by half a unit (i.e., $n\to n\pm1/2$), and this would produce a change $\Delta\mu_z/2$ of the magnetic moment, i.e., half of that produced for an equilibrium transition between two IF states .

Chapter 3

Materials and Methods

3.1. Crystal growth of Sr_2RuO_4

The bulk single crystals of Sr_2RuO_4 used for our experiments were grown at Kyoto University in Prof. Maeno's group [43]. A floating-zone method was used in a commercial image furnace equipped with double-elliptical mirrors, where melting is achieved by focusing a light on the sample without a crucible. The bottom end of a feed rod suspended from above is melted and subsequently connected to a seed material held from below. By lowering both the feed rods and seed material, a single crystal is grown continuously from the Ru-rich molten solution. In the standard solid-state reaction, the ceramic feed rod is made with a reaction between $SrCO_3$ and RuO_2, and it was necessary to use a feed rod that contained excess Ru to compensate for evaporation. It is also found important to minimize impurities such as Ba and Na in order to obtain optimal transition temperature. The seed material can be either sintered poly-crystals or a single crystal. Using the technique, the crystal size can be as large as $80 \times 4 \times 3$ mm^3 and of very high quality with T_c as high as 1.49K. By adjusting growth conditions the superconducting temperature could be controlled, and it is found that the crystals with very low levels of impurity and defects tend to have narrow transition width and low residual resistivity. Growth conditions define various phases that were observed [43]: while optimal condition is obtained when the nominal molar ratio $2N(\mathrm{Ru})/N(\mathrm{Sr}) \approx 1.15$, Ru metal phases are observed imbedded in the main Sr_2RuO_4 when $2N(\mathrm{Ru})/N(\mathrm{Sr}) \geq 1.2$; epitaxial-like intergrowth of $SrRuO_3$ on Sr_2RuO_4 when the oxygen pressure $P(O_2) \approx 0.3\,\mathrm{bar}$; eutectic growth of Sr_2RuO_4 and a new insulating compound of unknown composition, possibly $Sr_3RuO_{5+\delta}$. The crystals used in the present study were tested by Maeno group using X-rays and magnetic susceptibility measurements to be free of any of these phases.

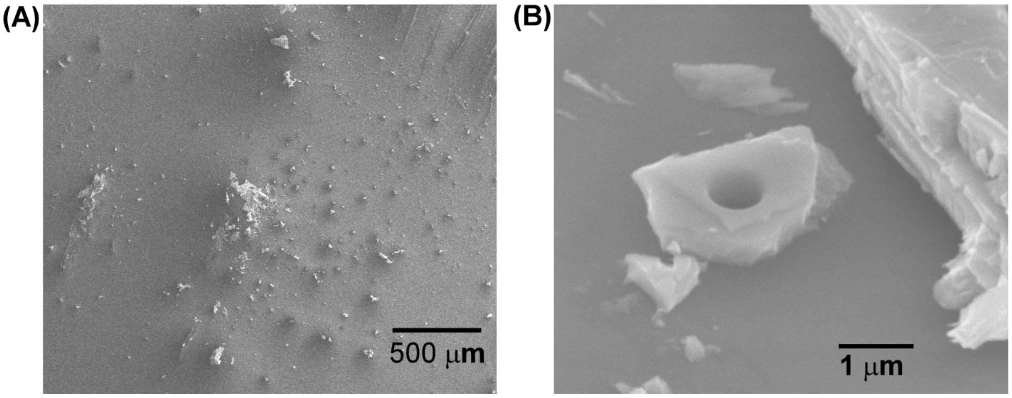

Figure 3.1 **(A)** Low magnification SEM of SRO debris field. **(B)** A micron-size SRO particle after cutting a hole using the FIB.

3.2. Sample preparation

The micron-sized annular Sr_2RuO_4 samples were obtained from millimeter-sized crystals grown using the floating-zone method. The SRO crystal was first glued to a post, then ~100-μm thick segments were cleaved using a razor blade. To avoid possible oxidation and surface contamination, only segments obtained from the interior of the larger crystal were used. The SRO segment was crushed on a silicon substrate and the pieces were imaged using the electron beam of a dual-column focused ion beam (FIB). Because of high anisotropy of the crystal properties, particle is cleaved fairly well along ab-plane, so that a millimeter size particle crushes into micrometer particles with well-defined crystal axis. The shape of the particles was found to be an important factor in determining the orientation of crystalline axis; for the particles used in this study, the orientation of the *ab*-planes was clearly visible from the layering observed near the edges of the particle. Figure 3.1 is an example of a low magnification SEM image showing the particle distribution (after crushing), which was later used as a map to identify the location of the FIB-ed particle under optical microscope. Higher magnification SEM scans from various angles were necessary to confirm the layering of a particle.

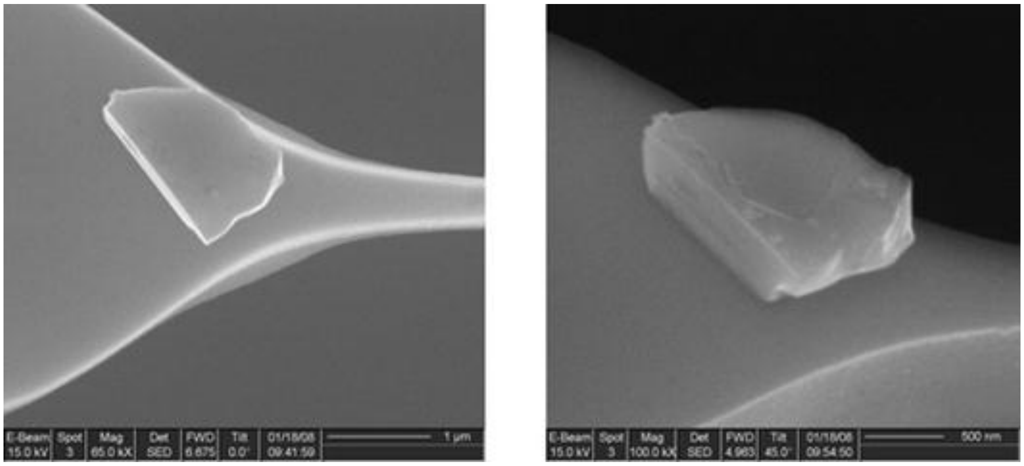

Figure 3.2 Particles on the cantilever.

After locating the desired particle, the 30 kV ion source was used to cut a hole in the center of the particle parallel to the crystal *c*-axis. In order to minimize ion implantation, the number of images taken using the ion source was limited to two exposures at emission current of 1 pA; the hole was cut using an emission current of 10 pA. The milled particle was then transferred to a micro-manipulator stage of a long working distance Mitutoyo optical microscope. The FIB-ed particle was located from the pattern of the debris field imaged using the SEM. A three-axis hydraulic Narishige micromanipulator was used to position a pulled borosilicate micropipette having a < 1 μm tip diameter near the particle. The electrostatic interaction of the particle with the micropipette was sufficient to pick up the particle. The particle was glued to the tip of a custom-fabricated silicon cantilever. Prior to placement of the particle, a small amount of Gatan G-1 epoxy (Gatan Inc., Pleasanton, CA, USA) was placed on the tip of the cantilever. The epoxy was cured overnight at 70 ℃ in a nitrogen environment. The planar geometry of the particle ensured that the particle's *c*-axis was oriented perpendicular to the axis of the cantilever. However, the *a* and *b* axes had no special orientation with respect to the cantilever.

3.3. Instrumentation and setup

3.3.1. Dewar and refrigerator

All experiments discussed in this text were performed in a continuous flow Helium-3 refrigerator (He-3-SSUHV-CF, Janis Research Company, Inc., Wilmington, MA, USA) inserted into a helium Dewar (Precision Cryogenic Systems, Inc., Indianapolis, IN, USA) equipped with a 6T magnet (Cryomagnetics Inc., Oak Ridge, TN, USA). The magnet is controlled with the Model CS4 Magnet Power Supply (Cryomagnetics Inc., Oak Ridge, TN, USA).

The magnet had a 6" bore which fit around the outside of the refrigerator's inner vacuum chamber. The Dewar was mounted on a vibration isolation table raised to 7 ft. high to allow a procedure of lowering down the Dewar to a pit with 6 ft. deep.

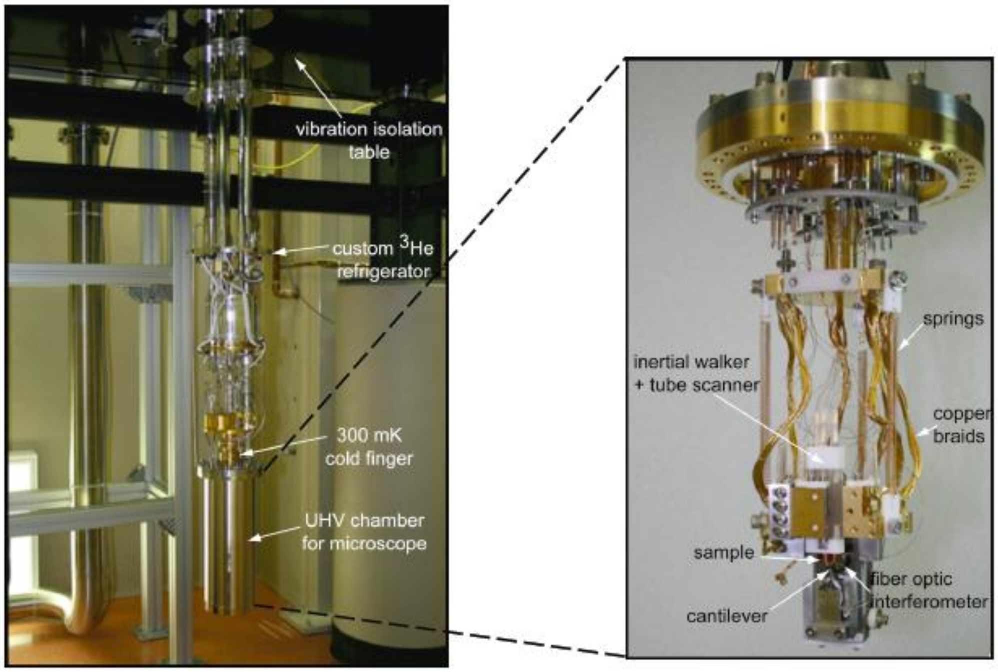

Figure 3.3 He-3 cryostat and sample stages.

A schematic of the refrigerator and Dewar is shown in Figure 3.3. The refrigerator was equipped with thermometers on its charcoal sorption pump, 1K pot, and helium-3 pot and with resistive heaters on the charcoal sorption pump and helium-3 pot. Additional thermometers (RX-202A, Lake Shore Cryotronics, Inc., Westerville, OH, USA) were glued with (Stycast-2850) onto the sample mounting stage using heat bobbins (Lakeshore Inc., Westerville, OH, USA) in order to ensure good thermal contact. The thermometers were measured and the heaters controlled by a piece of electronics from Lake Shore (Model 340 & 325 Temperature Controller, Lake Shore Cryotronics, Inc., Westerville, OH, USA). For the usual mode of operation of the refrigerator a reader should refer to the manual provided by Janis Inc.

A constant sample temperature was maintained by a PID feedback loop controlling a heater attached to the sample mounting manifold, while monitoring the sample stage thermometer. The feedback loop was implemented by the Lake Shore controller. The lowest temperatures were reached by allowing the 1K pot to fill completely, then closing the needle valve, and pumping on the 1K pot's exhaust line. A base temperature of ~310mK was achieved by this method with the cantilever detection apparatus mounted to the refrigerator.

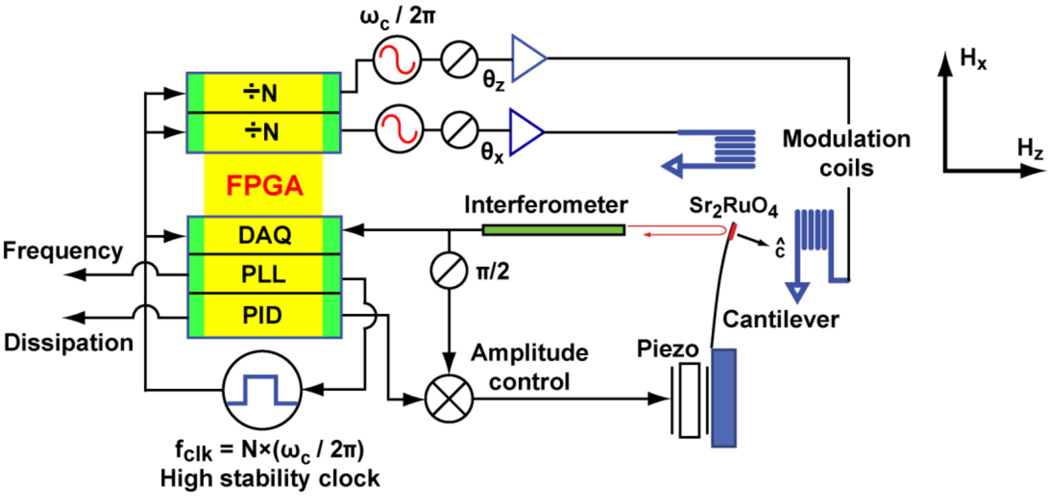

Figure 3.4 Schematic of phase-locked cantilever magnetometry apparatus.

3.3.2. Cantilever detection set-up

The basic cantilever detection set-up is shown in Figure 3.4. The cantilever motion is detected optically using a fiber-based interferometer [44]. The cantilever signal is converted to a voltage signal using a photodiode & tans-impedance amplifier (LMC6001) package and re-amplified with dc-coupled and ac-coupled SIM965 JFET (Stanford Research Systems) preamplifiers. The cantilever is mounted on a piezoelectric actuator which is driven resonantly by the amplitude control analog circuit, which also automatically adjust phase shift needed to drive the cantilever. Laser power was maintained by a control loop. We will now discuss each component of the set-up in more detail.

1) Laser source

The laser source used in all measurements was a 1510nm fiber-coupled diode laser from OKI (PL5109L-5A 5mW 1510 nm DFB Laser, OKI Optoelectronics, Japan) with built-in thermoelectric cooler and optical isolator. The laser was powered by a low noise current source (LDX-3620 Ultra-low noise current source, LightWave Inc., USA). Laser diode driver from Thorlab (LDC 240C) was, also, proved working fine without any additional noise. The driving current of the laser was approximately 17 mA for all measurements.

The laser wavelength was tuned via its temperature using a thermoelectric cooler embedded in the laser diode and home-made current supply operated by a LabView unit. We employed a constant RF modulation of the laser current in order to reduce optical feedback noise and optical interference noise [45]. The ~200MHz RF modulation signal was generated by a voltage-controlled oscillator (ZX95-400, Mini-Circuits, Brooklyn, NY, USA) which passed through a voltage-variable attenuator (5dB, Mini-Circuits, Brooklyn, NY, USA). The quiet interferometer signal is achieved by the reduction of interference between unwanted reflecting objects in the fiber interferometer path through the shortening of the laser coherence length. The un-shortened coherence length used of the laser is about several cm.

2) Fiber optic components

The optical beam path used to monitor the cantilever position is shown in Figure 3.4. The fiber coupled output of the laser was connected into a voltage controlled optical attenuator (MMVOV-1-1550-5-9/125-3A3A-0.25-1, OZ optics, Ottawa, Ontario, Canada) with a feed-back control loop on the output of the reference photodiode (In experiments in this paper, laser power impinges on the cantilever was maintained about 5 nW.) The attenuation also could be adjusted by hand by slightly unplug fiber connectors to change the laser power between measurements. The driving current of the laser was not varied to change the laser power. The attenuator output was connected to the input port of a 99:1 directional coupler (FFC-X142PB1XX-SFO572, JDS Uniphase, Milpitas, CA USA). The through port of the directional coupler was connected to a fiber-coupled photodiode package (FCI-InGaAs-70-SM-FC, Hawthorne, CA, USA) which we refer to as the reference photodiode. The coupled port of the directional coupler was connected to a long fiber which was fed into the inner vacuum chamber (IVC) of the cryostat and mounted with its end towards the cantilever to be detected. The vacuum feedthrough for the fiber uses a combination of a Swagelok connector and a machined Teflon piece, which has a thin hole with a diameter chosen to barely accommodate the outer diameter of the fiber. The design is a replication of the one from the paper by [46]. The signal port of the directional coupler was connected to another photodiode package identical to the reference photodiode's and is called the signal photodiode.

3) Optical fiber setup

The preparation of the termination of the fiber directed at the cantilever is done by a commercial optical fiber cleaver (S323, FITEL, Japan) after the buffer coating layer was carefully stripped from the end of the fiber. When the end surface of fiber is smooth, 4% of the light incident on the surface reflected. The fiber end is fed into a 14mm long, 129 μm inner diameter /1mm outer diameter borosilicate ferrule (BD ACCU-GLASS, St. Louis, MO, USA), which is pre-glued to the stainless tube using H74 epoxy. The stainless tube has a collimating lens (350450C00 coating:10238, LightPath, Orlando, FL, USA) at one end which is glued by a small amount of TorrSeal with a caution not to blur the surface of the lens. A precaution should be given to the way the ferrule is glued: in order to maintain the optical alignment through thermal contraction, two-point support is preferred over four-point support. One end of the ferrule has a tapered opening to allow the fiber to be fed in. When the fiber was inserted into the ferrule the tip of the fiber extended to the desired location, which is 1.6 mm away from the collimating lens, while the end of the buffer coating layer fit inside of the tapered ferrule lead-in. The fiber is epoxied into the stainless tube using TorrSeal. Then, the tube was inserted to a fiber positioner and fixed to the sample mounting manifold.

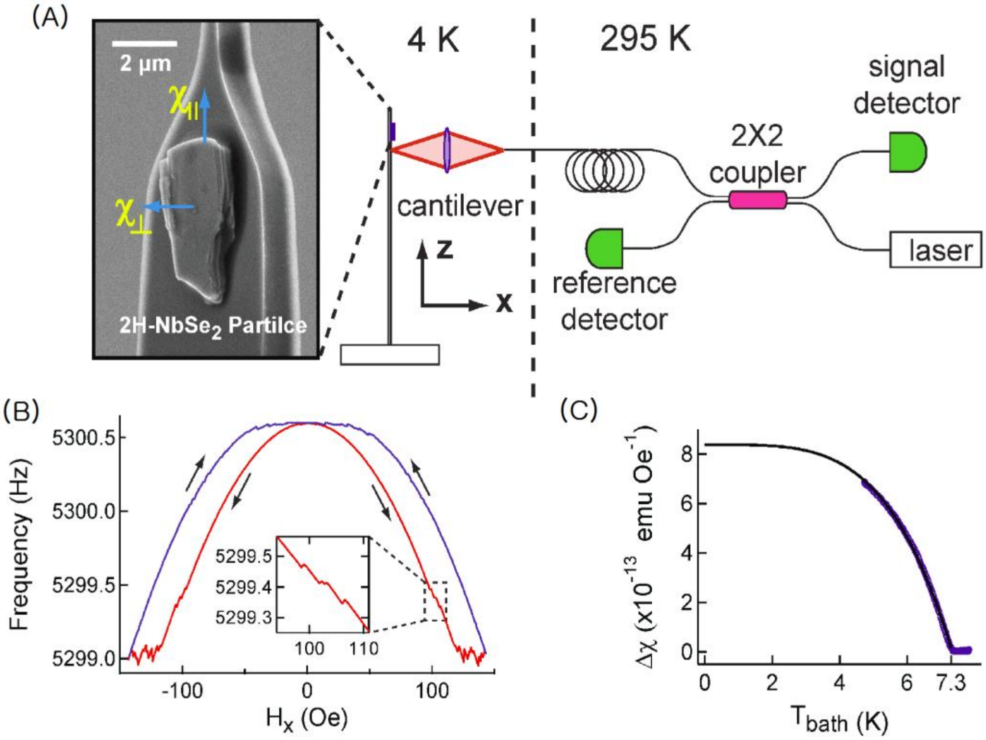

Figure 3.5 Schematics of experimental setup. (A) Optical path of the laser interferometer is shown with a SEM micrograph of a $NbSe_2$ particle and cantilever head. Shown in (B) is a typical cantilever frequency shift response to the external magnetic fields. (C) Magnetic susceptibility of the particle is plotted in function of temperature.

4) Cantilever holder

Cantilever chips were held to a springboard structure made of stainless, and the tension of the structure is maintained by a Piezo-actuator (EBL#4, EBL Products Inc. East Hartford, CT, USA) and a set screw. A sapphire disk is used to preprevent damage on the Piezo by the set screw. A thermometer is glued very close to the chip to ensure thermal equilibrium. A millimeter-size field coil is hand-wound with 4 mil NbTi Cu-clad wire, and glued with G-1 epoxy (Gatan) to a pocket positioned 500 μm from the chip. All wiring including copper needs to be heat-sinked to the 0.3K cold finger using the copper bobbin to ensure good thermal contact.

5) Electronics and control

For measurements of the cantilever frequency, the output of the signal photodiode was fed into the input port of dc and ac preamps (SIM910 JFET, Stanford Research Systems, Sunnyvale, CA, USA). The output signal of the ac preamp goes to a band pass filter (SIM 965 Analog filter) with $\pm 2\,\text{kHz}$ about the cantilever frequency, and digitized by Field Programmable Gate Arrays (FPGA, Pxi-7833R, National Instrument) for the frequency measurement by the Phase Lock Loop (PLL). PLL processes the digitized interferometer signal by multiplying a square wave, low-passing it, and feeding back to local oscillator (Agilent 33220A Function generator) to match the frequency of the square wave to the cantilever signal. Core processes, including the frequency measurement, fringe locking and amplitude control, are done with FPGA. Electronics and instruments are controlled using LabVIEW, which was also used to control current supplies for magnetic fields and record all the readings of all other electronic components during the experiment.

3.4. Cantilever magnetometry

The mechanical detection has an advantage of having a clean electromagnetic environment and straight forward interpretation of the signal. The absence of an electronic probe guarantees undistorted external fields throughout the sample and become minimally intrusive. That simplifies the interaction between sample, mechanical oscillator and measurement system, which allows us to observe the delicate quantum phenomena. Data in this section were also reported in [47].

3.4.1. Introduction

One of the most notable scientific achievements with magnetometry involving mechanical detection was the precise measurement of the de Haas-van Alphen effect, which led to the important experimental confirmation of the Fermi surface. Modern style cantilever magnetometry was emerged in the 1980s, mainly thanks to technical advances in micromachining of previous decades. These advances allowed for the fabrication of single crystal mechanical oscillators with very high quality factors and led to the subsequent development of the atomic force microscope (AFM) [48].

The earliest applications of the cantilever magnetometry include magnetic force microscopy and studies of flux lattice melting in high temperature superconductors by cantilever torsional magnetometer. Many the pioneering works on cantilever magnetometry were performed by Dan Rugar and collaborators at IBM for magnetic resonance force microscopy (MRFM). Their achievement include the detection of the magnetic moment of single electrons [49] and manipulations of small ensembles of spins [50]. They represent considerable progress in detecting ultra-small forces, down to the a few attonewton. Besides the MRFM, another research area that benefits from ultrasensitive force detection is the cantilever-based magnetometry, which is the main technique used in the research of this paper.

The cantilever-based detection offers higher sensitivity and a cleaner electromagnetic environment than other approaches. In most of applications, however, high detection sensitivity is achieved by applying large magnetic fields. Such an approach is not well suited for determining the low-field magnetic response of a sample, which motivated us to the development of the phase-locked measurement. Basic principles of cantilever force detection scheme will be presented. We mostly focus on dynamic measurements where the detection makes use of the fundamental flexural mode of vibration.

3.4.2. Ultrasensitive cantilevers

Nano-fabricated cantilevers can be used as transducers that convert force signals into displacement. If thermal vibrations are the dominant noise source, as is usually the case for very soft cantilevers, then the force noise is determined by the dissipation in the cantilever defined by the fluctuation-dissipation theorem. The thermo-mechanical noise is often analyzed by approximating the cantilever dynamics using a simple harmonic oscillator with a Langevin thermal noise term $F_{noise}(t)$:

$$m\frac{d^2x}{dt^2}+\Gamma\frac{dx}{dt}+kx=F_{signal}+F_{noise}(t)$$

,where x is the displacement at the tip, m is the cantilever effective mass, k is the cantilever spring constant and Γ is the friction coefficient that characterizes the dissipation. For a cantilever with resonance frequency ω_0 and quality factor Q, then $\omega_0^2=k/m$ and $\Gamma=k/\omega_0 Q$.

In order to maintain thermal equilibrium, the spectral density of the force noise S_F must depend on the cantilever dissipation according to the fluctuation-dissipation theorem such that

$$S_F = 4\Gamma k_B T.$$

For detection in a bandwidth B, this spectral density gives the minimum detectable force

$$F_{min} = S_F^{1/2} B^{1/2} = \left(\frac{4kk_B TB}{\omega_0 Q} \right). \qquad (3.1)$$

In case of oscillating the cantilever and detecting changes in cantilever resonance frequency, the thermo-mechanical noise limit of the frequency detection becomes [51]

$$\Delta\omega_{min} = \frac{F_{min}}{2kx_{rms}} \omega_0,$$

where x_{rms} is the root-mean-square oscillation amplitude.

So, we gain better force sensitivity either reducing the dissipation Γ or by lowering the temperature. In the continuous flow He-3 cryogenic system, we achieved cantilever's temperature ~350mK by implementing good thermal contacts and minimizing the laser power to a few nanoWatt for less optical absorption. The dissipation Γ generally becomes smaller as temperature decreases, and also depends on cantilever geometry and material properties. For the fundamental flexural mode of a simple rectangular cantilever, $k = 0.258Ewt / L^3$ and $\omega_0 = 1.015(t / L^2)(E / \rho)^{1/2}$, where E is the Young's modulus of the cantilever material, ρ is the density of material and L , w, and t are the length, width and thickness, respectively [52]. Combining these, we find

$$\Gamma = 0.254 \left(\frac{wt^2}{LQ} \right) (E\rho)^{1/2}.$$

It should be noted that for nanometer size resonators, Q decreases with size because of various contaminations and oxidations at the cantilever surfaces; thus, extra attention is paid to keep surface clean to maintain high Q cantilevers. Combined with the above formula and the fact that the quality factor Q is generally only a material property, independent of geometry, Γ is minimized by making the cantilever narrow (w), thin (t) and long (l).

The cantilevers used in our experiments, made in the Stanford Nanofabrication Facility by Banjamin Chui and Trevis Crane, were fabricated from a (111)-oriented silicon-on-insulator wafer and was hydrogen-passivated to avoid oxidation. The backside etch through the silicon substrate was performed using an anisotropic deep reactive ion etching process. The cantilever was then released from an encapsulating oxide using vapor HF etch and then dried in a CO_2 critical point drier to avoid problems of surface tension. The cantilevers are always maintained in a nitrogen dry box and expose to air is minimized by quickening the setup procedures.

3.4.3. Optical interferometry and operations

1) Fringe lock and calibration

Displacement of the mechanical oscillator is measured interferometrically by coupling a 1510-nm distributed feedback diode laser to the 99/1 fiber optic coupler. The 100-nm-thick Si paddle (30% reflectance at $\lambda = 1.5\,\mu m$) and the cleaved end of the fiber (4% nominal reflectance) form Fabry-Pérot (FP) optical cavity with *finesse* ~1. In the limit of very low *finesse*, only one reflection from the cantilever is accounted for the interference. We call the distance from the point of reflection in the fiber (either the Bragg reflector or the cleaved fiber end) to the cantilever surface at equilibrium x_0, and we call the cantilever displacement from equilibrium x_1.

Optimal interferometer fringe position and laser wavelength tuning is done as follows. The cantilever interferometer signal when plotted as a function of wavelength λ or cavity length x_0 is known as the interferometer "fringe." The condition $x_0 = \lambda(n+1/4)/2$ maximizes the slope of the fringe and maximizes detection sensitivity. The interferometer signal to displacement conversion can be done by assuming the shape of the fringe sinusoidal, which is good approximation in most cases. The slope at the midpoint of the fringe should be given by the fringe maximum voltage V_{max} and minimum voltage V_{min} . With an assumption of a unity gain of the interferometer signal the conversion factor is given as

$$c_f = \frac{2}{\pi} \frac{\lambda/4}{V_{max} - V_{min}}.$$

2) Determination of resonant phase for the cantilever drive signal

For the cantilever frequency measurements, the cantilever was driven in a phase-locked loop using the arrangement described in Figure 3.4. In this set-up, an analog circuit for amplitude control drives the cantilever using the cantilever interferometer signal as its reference. The circuit also maintains a fixed phase between its reference and the cantilever drive signal, effectively adjusting its output frequency. On resonance, a simple harmonic oscillator's motion is 90◦ out of phase with its drive; however, due to extra phase shifts from the leads, filters, and amplifiers in the phase-locked loop, the reference phase required to drive the cantilever often differs from 90◦.

In order to find the resonant phase, the frequency of free ring-down is compared to the driven frequency. When the phase is right, the frequencies match and consistently the driving becomes most efficient. This can be done very accurately using an oscilloscope: you manually trigger the driven signal to be looking stationary on the monitor, then stop the driving to observe the movement of the free ring-down. If the phase is 90◦, the ring-down signal will be looking stays at the same location. In practice, while measuring quality factor of the cantilever, the ring-down frequency can be measured using a zero-crossing-count method, thus readily compared to the ready-recorded driven frequency.

3.4.4. Measurements of force noise

For calculating minium detectable force by a cantilever, we need to know spring constant k, temperature T, resonant frequency ω_0 and quality factor Q. The interferometer to monitor the cantilever vibration noise at a known point at the shaft of the cantilever. By taking account of the mode shape of cantilever vibration, we can extract the root-mean-square tip displacement x_{rms}, which represent an amplitude of the cantilever vibration noise corresponding to the fundamental mode of vibration.

x_{rms} can be interpreted in terms of an “effective” cantilever temperature according to $T_{eff} = kx_{rms} / k_B$. At room temperature, T_{eff} is found to accurately track the temperature of thermal noise at room temperature to estimate the cantilever spring constant. However, at low temperatures, X_{rms} can sometimes be larger than expected (i.e. T_{eff} >T) due to external vibrations, laser heating of the cantilever or detector noise. To determine $S_F^{1/2}$, these extra noise sources need to be included. We do this by substituting T_{eff} for T in , which leads to an expression that depends explicitly on the measured vibration noise :

$$S_F^{1/2} = \left(\frac{4}{\omega_0 Q} \right)^{1/2} kx_{rms}$$

The optical absorption is significantly reduced by using a laser whose the photon energy is less than the silicon bandgap. Also, reflectivity from the silicon cantilever can be optimized by adjusting the thickness, satisfying constructive interference for the reflecting waves. For $\lambda = 1510$ nm very good reflectivity is obtained with a 100nm thick bare silicon cantilever because the large index of refraction of silicon (n ~3.5) ensures the phase difference of 2π.

3.4.5. Passive dynamic detection

In dynamic detection, one measures the change in the cantilever frequency or dissipation in response to the externally applied field. During measurement, the cantilever is placed in a positive feedback loop and is driven at its natural frequency ω_c using a piezoelectric transducer; the resulting tip motion is given by $z(t) = z_{pk} \cos \omega_c t$. A digital controller implemented in a FPGA maintains constant tip amplitude z_{pk} and is also used to determine both the instantaneous cantilever frequency and dissipation.

In the presence of external fields, the magnetic moment $\vec{\mu}$ produced by superconductor generates a torque $\vec{\tau} = \vec{\mu} \times \vec{H}$ which acts on the cantilever. By expanding the z-component of the resulting force, and keeping terms linear in the cantilever displacement, the Fourier transform of the linearized equation of motion for the cantilever is obtained.

$$(-\omega^2 + i\gamma\omega + \omega_0^2)\tilde{z}(\omega) \approx \frac{\omega_0^2}{kL_e^2} \mu_z H_z \tilde{z}(\omega). \qquad (3.2)$$

Here, ω_0, k and γ are the cantilever frequency, spring constant and dissipation in the absence of magnetic interactions; $L_e \approx L/1.38$ is the effective length of the cantilever. The term on the right-hand-side of Eq.(3.2), which we refer to as the passive dynamic force, relies on the bending of the cantilever to generate an oscillating magnetic field $H_x \approx H_z z / L_e$ in the reference frame of the superconductor; the resulting position-dependent force shifts the cantilever frequency. Expressing the field dependence of μ_z indicated above and assuming the c-axis susceptibility $\chi_z = \partial\mu_z / \partial H_z$ to be constant gives $\Delta f_P \approx f_0(\chi_z H_z^2 + \Delta\mu_z n H_z) / 2kL_e^2$, where $f_0 = \omega_0 / 2\pi$ and $\Delta\mu_z$ is the z-component of the jump in moment caused by vortex entry. Note, in writing Eq. (3.2) we have assumed that $\chi_z >> \chi_x$ and neglected the contribution to the torque from χ_x. This assumption is justified because of the large shape anisotropy of our sample as well as the highly anisotropic response of the superconductor. Again in Sr_2RuO_4, $\lambda_{ab}(0) = 152nm$, $\lambda_c(0) / \lambda_{ab}(0) \approx 20$, where $\lambda_{ab}(0)$ and $\lambda_c(0)$ refer to the zero temperature in-plane and c-axis penetration depths.

The dynamic magnetometry offers a number of advantages. First, operating at the resonant frequency enhances displacement sensitivity of the oscillator by the quality factor Q and greatly facilitates thermal limited force detection. Second, variations in the cantilever frequency caused by changes in μ_z can be tracked instantaneously. If we calculate the magnetic moment sensitivity, however we find that the spectral density of moment fluctuations for passive dynamic detection $\left(\sqrt{S_\mu}\right)_{passive} = \left(\sqrt{S_\mu}\right)_{static} (L_e / z_{pk})$ is larger by a factor of L_e / z_{pk} than for static torque measurement $\left(\sqrt{S_\mu}\right)_{static} = \sqrt{S_F} L_e / H_z$; here, $\sqrt{S_F} = \sqrt{4k_B Tk / \omega_0 Q}$ is the spectral density of thermal force fluctuations. For our experimental parameters $L_e \approx 55 \mu m$ and $z_{pk} \approx 60 nm$, the reduction in sensitivity $z_{pk} / L_e \sim 10^{-3}$ is significant. Phase-locked magnetometry overcomes this limitation by using an active approach to directly apply a position-dependent field. Thus, for the same magnitude of the applied field, the detection sensitivity is enhanced by a factor of L_e / z_{pk} relative to passive dynamic measurement.

3.4.6. Phase-locked detection technique

In this section, we describe a feedback-based dynamic cantilever magnetometry technique capable of achieving high magnetic moment sensitivity with low applied fields. Using this technique, we have observed periodic entry of vortices into mesoscopic Sr_2RuO_4 rings. The quantized jump in the magnetic moment of the particle produced by individual vortices was measured with a resolution of $7\times10^{-16}\,emu$ at an applied field of 1 G.

In the presence of an external magnetic field $\boldsymbol{H}$, the cantilever is subject to a torque $\boldsymbol{\tau}=\boldsymbol{\mu}\times\boldsymbol{H}$ produced by the magnetic moment $\boldsymbol{\mu}(\boldsymbol{H})$ of the superconductor. During measurement, the cantilever is placed in a positive feedback loop, and is driven at its natural frequency using a piezoelectric transducer; the resulting tip motion is given by $z(t)=z_{pk}\cos\omega_c t$. To enhance detection sensitivity, a small time-dependent magnetic field $\Delta\boldsymbol{H}(t)$ is applied perpendicular to the component of $\boldsymbol{\mu}$ that we seek to detect. By making $\Delta\boldsymbol{H}(t)$ depend on the phase of the cantilever position, the cantilever experiences a dynamic position-dependent force, which shifts either the cantilever frequency or its dissipation. In general, the applied modulation can be of the form: $\Delta H(t)=\Delta H_{\mathrm{x}}\cos(\omega_c t+\theta_{\mathrm{x}})\hat{\mathrm{x}}+\Delta \mathrm{H}_{\mathrm{z}}\cos(\omega_{\mathrm{c}}\mathrm{t}+\theta_{\mathrm{z}})\hat{\mathrm{z}}$, where the phase angles θ_{x} and θ_z can be independently chosen. We refer the reader to a more detailed treatment of phase-locked cantilever magnetometry in ref. In the presence of a static magnetic field $\boldsymbol{H}=H_{\mathrm{x}}\hat{\mathrm{x}}+H_z\hat{z}$ and the applied modulation $\Delta\boldsymbol{H}(t)$, the Fourier transform of the equation of motion of the cantilever is given by:

$$\left(-m\omega^2 - im\gamma\omega + k\right)\tilde{z}(\omega) = \frac{1}{L_{eff}^2}\left\{\left(\mu_{\mathrm{x}} - \chi_c H_{\mathrm{x}}\right)H_{\mathrm{x}} + \left(\mu_z - \chi_{ab}H_z\right)H_z\right\}\tilde{z}(\omega)$$

$$+\frac{1}{L_{eff}\,z_{pk}}\left\{\left(\mu_{\mathrm{x}} - \chi_c H_{\mathrm{x}}\right)\Delta H_z e^{i\theta_z} + \left(\mu_z - \chi_{ab}H_z\right)\Delta H_{\mathrm{x}} e^{i\theta_{\mathrm{x}}}\right\}\tilde{z}(\omega). \quad (3.3)$$

Here, k, $m = k/\omega_c^2$, and $L_e(\approx L/1.38)$ are the cantilever spring constant, effective mass and effective length, respectively; μ_{x} and μ_z are the *c*-axis and *ab*-plane components of the magnetic moment and χ_c and χ_{ab} are the two components of the magnetic susceptibility of the sample. We note that for our samples $\chi_c \gg \chi_{ab}$. In our measurements, $L_{eff} \approx 55\,\mu\mathrm{m}$ and $z_{pk} \approx 60\,\mathrm{nm}$, thus the assumption of small angles is justified. The static magnetic fields applied in the lab reference frame generate position-dependent fields in the oscillating reference frame of cantilever in addition to the applied modulation. To ensure that the magnetic field in the reference frame of the SRO sample has the desired time-dependence, both feedback and feed-forward modulation is applied in the x and z directions.

To measure the *c*-axis moment, we modulate the in-plane field by $\delta H_{\mathrm{x}} = 1.0\,\mathrm{Oe}$; the relative phase is chosen so as to shift the cantilever dissipation γ: $\theta_{\mathrm{x}} = \pi/2$. An expression for the shift in dissipation is obtained from Eq. (3.3)

$$\Delta\gamma_z = \frac{\omega_c}{kL_{eff}\,z_{pk}}\delta H_{\mathrm{x}}\left(\mu_z - \chi_{ab}H_z\right) \quad (3.4)$$

In the regime that the superconductor exhibits linear response, $\mu_z = \Delta\mu_z n + \chi_c H_z$, where n is the fluxoid quantum number and $\Delta\mu_z$ is the change in the magnetic moment of the ring associated with fluxoid entry. Since $\chi_c \gg \chi_{ab}$, Eq. (3.4) reduces to

$$\Delta\gamma_z \approx \frac{\omega_c}{kL_{eff}\,z_{pk}}\delta H_{\mathrm{x}}\left(\Delta\mu_z n + \chi_c H_z\right).$$

To measure the *ab*-plane moment, we modulate the *c*-axis filed by $\delta H_z = 1.0$ Oe; the relative phase is also chosen to be $\theta_z = \pi / 2$. The expression for the shift in dissipation is given by

$$\Delta\gamma_{\mathrm{x}} \approx \frac{\omega_c}{kL_{eff}\, z_{pk}}\left(\mu_{\mathrm{x}} - \chi_c H_{\mathrm{x}}\right)\delta H_z \ . \tag{3.5}$$

The phase-locked cantilever magnetometry technique can also be used to measure the derivative $d\mu / dH$; derivative measurements are particularly useful in studying non-hysteretic magnetic variations; under certain conditions, derivative measurements can yield higher signal-to-noise ratio than the direct measurements of magnetic moment discussed above. In this work, we employ derivative measurements to study the high temperature behavior of the fluxoid transitions. For the derivative measurements, a small phase-locked modulation $\delta H_z(t)$ is applied parallel to the *c*-axis of the sample. In the presence of a non-zero static in-plane magnetic field H_x, the position-dependent magnetic moment produced by $\delta H_z(t)$ shifts the cantilever dissipation by

$$\Delta\gamma_{\mathrm{x}} \approx \frac{\omega_c}{k\,L_{eff}\, z_{pk}}\left(\mu_{\mathrm{x}} - \chi_c H_x\right)\delta H_z$$

If we neglect the term $d\mu_{\mathrm{x}} / dH_z$, and provided the modulation amplitude is sufficiently small, the above equation reduces to

$$\Delta\gamma_{\mathrm{x}} \approx -\frac{\omega_c}{k\,L_{eff}\ z_{pk}}\left(\frac{d\mu_z}{dH_z}\right) H_{\mathrm{x}}\ \delta H_z$$

Here, we have expressed χ_c as $d\mu_z / dH_z$. We see from the above equation that it is possible to measure the derivative of the out-of-plane magnetic moment $d\mu_z / dH_z$ with high precision provided H_{x} is sufficiently large.

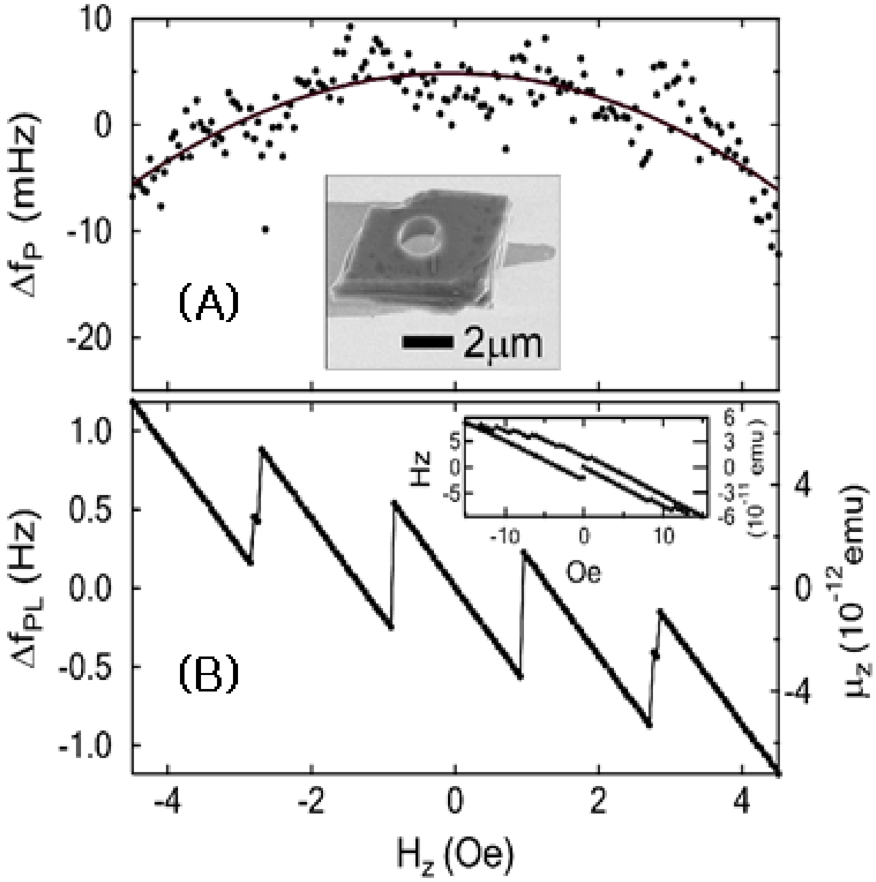

Figure 3.6 Comparison of (A) passive dynamic detection and (B) phase-locked detection.

Figure 3.6 shows passive dynamic magnetometry data $(\delta H_x = 0)$, taken at $T = 0.6K$ for a ruthenate particle having dimensions 5 μm ×4 μm ×2 μm with a 1.8 μm diameter hole in the center. For both parts (a) and (b) of the measurement, the equilibrium state of the superconductor is realized by increasing the laser power to momentarily heat the particle above T_c, then cooling below T_c in the presence of an external field (field cooling). We find that the frequency response in Figure 3.6 (a) exhibits a quadratic dependence on H_z indicative of the Meissner response, however the jumps associated with vortex entry cannot be resolved at low fields.

Figure 3.6 (b) shows the same field sweep taken using phase-locked detection. For this data $\theta_x = 0$, and the cantilever frequency shift is given by $\Delta f_{PL} \approx f_0(\chi_z H_z + \Delta\mu_z n)\delta H_x / 2kL_e z_{pk}$. The data taken with $\delta H_x = 1.3\,Oe$ clearly shows the linear Meissner response as well as the quantized jumps in magnetization related to periodic entry of vortices into the hole. To estimate the magnitude of the jump, we consider the change in magnetic moment of the particle $\vec{\mu} = \frac{1}{4\pi}\int(\vec{B} - \vec{H})dV$ upon vortex entry. For this annular particle, whose radius R, wall thickness d and length L, are all large compared to λ_{ab}, the change in magnetic moment can be easily estimated $\Delta\mu_z \sim R^2 L\Delta B / 4 = \phi_0 L / 4\pi$, where ΔB is the change in magnetic field inside the hole and $\phi_0 = 2\times10^{-7}\,Gcm^2$ is the magnetic flux quantum. Based on the dimensions of the ring, the estimated jump $\Delta\mu_z \sim 3\times10^{-12}\,emu$ is in reasonable agreement with the measured value $\Delta\mu_z \sim 5\times10^{-12}\,emu$. From the slope of the data between jumps, we find $\chi_z = 3.8\times10^{-12}\,cm^3$. We also calculate the average slope over the ±4.5 Oe range of the data, which gives $\bar{\chi}_z = 1.1\times10^{-12}\,cm^3$; this value is in good agreement with the value $\bar{\chi}_z = 1.2\times10^{-12}\,cm^3$ determined from the quadratic fit to the data in Figure 3.6 (a).

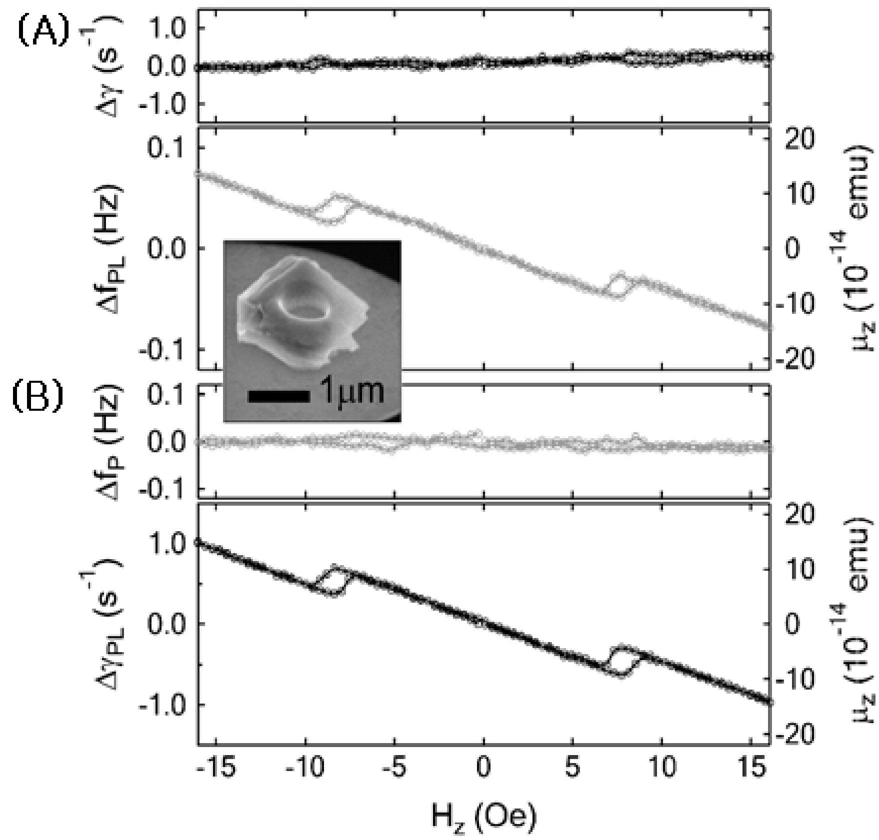

Figure 3.7 Magnetic signal appeared on (A) frequency and (B) dissipation of a cantilever

Figure 3.7 shows data taken by cyclic field sweep starting from $H_z = 0$ at a constant temperature of $T = 0.5K$. Phase-locked measurements were obtained in two modes: (a) $\theta_x = 0$ (frequency shift) and (b) $\theta_x = \pi / 2$ (dissipation shift.) For mode (b), the shift in dissipation and the magnetic moment are related by $\Delta\gamma_{PL} \approx -\omega_0(\chi_z H_z + \Delta\mu_z n)\delta H_x / kL_e z_{pk}$. Notice that the measured magnetization is nearly identical for both modes. Mode (b) has the added benefit in that it allows the passive and phase-locked signals to be separately measured. From the standard deviation of the data in Figure 3.7 (b), we determine the moment sensitivity within the $\tau_m = 1s$ integration time of the measurement to be $\Delta\mu \sim 7 \times 10^{-16}\, emu$. Based on the cantilever parameters, we find the measured moment sensitivity is near the theoretical limit $\Delta\mu = L_e\sqrt{S_F \Delta\nu} / \mu_0 \delta H_x \sim 5\times 10^{-16}\, emu$, where $\Delta\nu = 1/2\tau_m$ is the equiva- equivalent noise bandwidth corresponding to a time record of length τ_m.

Chapter 4

Search for the chiral edge current

The observation of the chiral edge current will give evidence that the order parameter has broken time-reversal symmetry. Although any time-reversal symmetry broken state may show the edge current, the group theoretic analysis and energetic considerations suggest that $\mathbf{d} = \mathbf{z}(p_x \pm ip_y)$ is the most likely phase to happen. Such chiral states have been predicted to carry spontaneous edge-currents of magnitude 5.6×10^{-6} A per layer [31]. If the sample has a single chiral domain, then the combination of the chiral currents and the Meissner screening currents would produce an additional magnetic moment. However, to within the noise resolution of the experiment, the field-cooled magnetization curve shows no signature of a zero-field moment.

Data presented here was taken from several crystals with various size and shape. This fact strengthens our conclusion that the chiral edge currents are much smaller than what is predicted by previous theoretical analysis. We will detail the experimental conditions and results, and discuss possible explanations regarding the order parameter of the Sr_2RuO_4.

4.1. Order parameter of Sr_2RuO_4

The superconducting phases with the fully gaped, unitary order parameter are energetically favored over non-unitary or nodal phases. On the other hand, it should be noted that among the five possible unitary states that lack symmetry required nodes, the state with order parameter $\mathbf{d} = \mathbf{z}(p_x \pm ip_y)$ is the only chiral state and has their equal spin pairing (ESP) axis in-plane, a necessary condition to be consistent with the results in Chapter 5. Such chiral states have been predicted to carry spontaneous edge-currents. While the gap function with the order parameter is fully gapped, the measurements of the magnetic penetration depth, NMR relaxation time, and thermal conductivity might suggest a line node. Thus, the $p_x + ip_y$ phase is still debatable, and the possibility of line nodes in the order parameter can be ruled out if the chiral current is measured.

The edge current is the consequence of the non-zero angular momentum of the Cooper pairs [28]. Phenomenologically speaking, the current is generated in consequence of the order parameters varying near edges. That's because in the complex multi-component Ginzburg-Landau equations, the relationship between current and order parameter become "tensorial". Therefore, when order parameter changes perpendicular to edges the current can flow parallel to the edges [16]. In general, any local perturbation of the chiral p-wave order parameter results in supercurrents. Thus, equilibrium spontaneous supercurrents are expected to flow at the defects and edges of a sample, confined to within a coherence length ξ. In a superconductor, however, this current is to be screened by the Meissner effect, and the magnetic field inside the superconductor vanishes. Consequently, there will be an opposite screening current flows confined approximately to within the penetration depth λ from the surface. Due to the different spatial distributions of these two currents, there is a net magnetic field at the surface, which is predicted to have a maximum value of about 10 G in an idealized model [31].

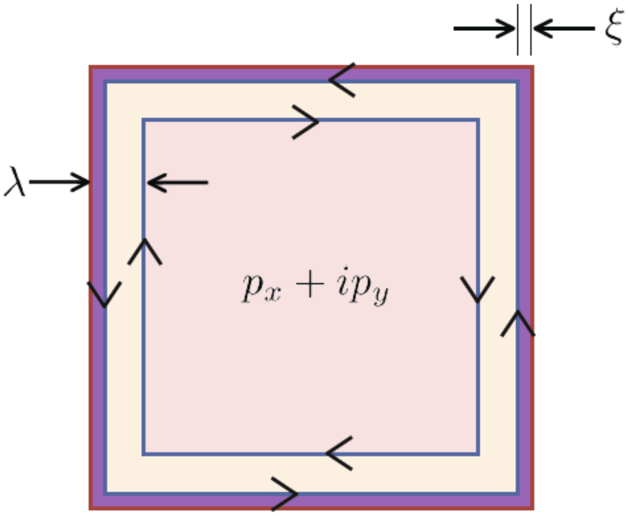

Figure 4.1 A simplified picture of spontaneous chiral edge currents and Meissner screening currents.

Moreover, due to the discrete symmetry of the 2-d layered structure the order parameter is expected to have two degenerate phases with $p_x + ip_y$ and $p_x - ip_y$ with formation of domain walls to separate the phases. Similar supercurrents and fields result at domain walls. The field alternates in sign across a domain wall and achieves a bigger field of about 20 G, but on average the magnitude would be smaller. Note that the μSR experiment is interpreted as evidence for internal fields associated with this domain wall currents [18]. However, the domain walls cost energy due to the current generated by it and the suppression of order parameters. In principle single domain over a sample is energetically favorable, but natural inhomogeneity of sample, such as defects and impurities, and non-zero external fields might trigger multiple domains separated by domain walls. Recently, there were Josephson junction measurements, showing odd parity of the order parameter and micron size multiple dynamic domain structure [53] and polar Kerr rotation measurement shows TRS breaking [19]. However, the different experiments indicate possible domain size ranging from 1 μm to 50 μm.

4.2. Estimation of magnitude

The field generated by the domain wall and edge current, which is confined within coherence length ξ, is screened by Meissner current flowing within a length scale of penetration depth λ. Thus, the actual spontaneous current will be confined within $(\xi - \lambda)$ from the walls and edges, which was accounted self-consistently in the quasi-classical calculation by Matsumoto and Sigrist [31].

Our ability to measure magnetic response in low field comes as an advantage because it makes us able to distinguish the domain dynamics from vortex dynamics. It is always desirable to eliminate the effect of vortex dynamics, which can give some confusion in the interpretation. We have enough measurement sensitivity below $\mu_0 H_{c1}$ parallel to c-axis which is about 50G.

Following the self-consistent calculation of Matsumoto et al. for current distribution at superconductor-insulator interface, a simplified picture is that the domain has finite angular momentum to z-axis to generate chiral current flowing counter-clockwise. Because there is always Meissner current shielding magnetic field inside of the superconductor the counter current flow clockwise to eventually compensate the current to give zero magnetic field inside bulk. The resultant current configuration assuming single $p_x + ip_y$ domain and rough estimation of the magnetic moment from the current are given in Figure 4.2. Indeed, it would be considerably above the minimum detectable moment.

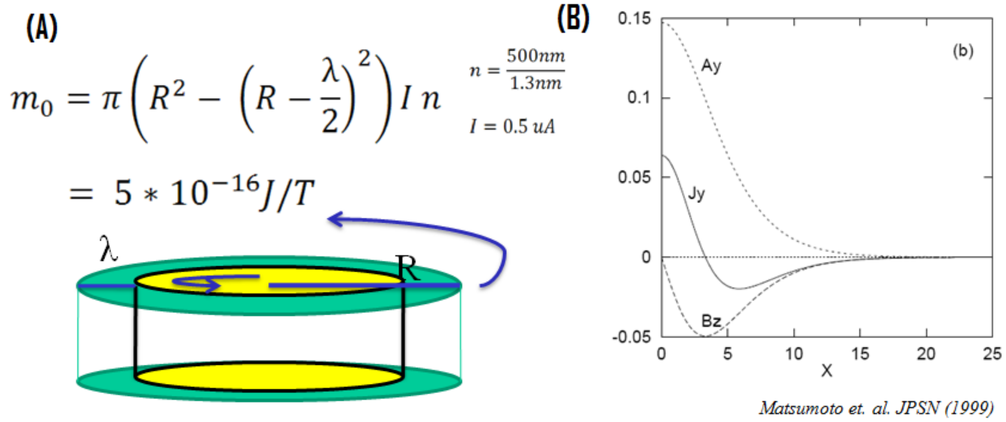

Matsumoto et. al. JPSN (1999)

Figure 4.2 : (A) Simplified calculation for the edge current using a disk geometry. (B) Matsumoto-Sigrist calculation using quasiclassical Green function method.

To be more quantitative, numerical integration of Matsumoto-Sigrist calculation performed.

Given $\xi_0 = 66nm$, $v_F = 5.5\times10^4 ms^{-1}$, $N(E_F) = 4.36\,\text{states/eVcell}$ and $T_c = 1.5K$, the expected magnetic moment would be

$$m_0 = 3.8\times10^{-27}\times ev_F N(0) k_B T_C = 3.8\times10^{-27}\times1.18\times10^{11} = 5\times10^{-16} J/T \quad .$$

$$= 5\times10^{-13}\ \text{e.m.u.}$$

We need to emphasize the assumption that domain size is comparable to size of sample dimension. If that is not the case, the expected magnitude of the signal would be smaller. More discussions will be presented in the last section.

4.3. Experimental conditions

We glued particles whose diameters range from 1.3 μm to 4 μm on cantilevers, and measured fluctuation of magnetic moments and locations of vortex entries. From the Josephson junction and SQUID microscope experiments, it is suggested that the order parameter domain sizes would be of order of 1 μm or less. Thus, we expect that there will be only a few domains in the crystal. To search for evidence of chiral domains, we measured the magnetic moment of the sample after repeated field-cools. If the domain structure were to vary between the different field-cools, we would expect to observe deviations of the expected linear Meissner response. The field cool was performed by heating sample with the optical absorption from the interferometer laser, and subsequently cooling down temperature by decreasing the laser power. Note that the heating and cooling speed is very fast as the whole procedure is done within a few seconds, and is considerably faster than 1mK/sec rate used in previous similar experiments [20,54]. In addition to the static field, a 1G AC field at the cantilever frequency was applied to the sample during the field-cools. We assume that the oscillating magnetic field doesn't affect the dynamics of the order parameter domains. Another condition possibly affecting the domain formation is the earth magnetic field, which is about 0.5 G. Because the field is static in the time scale of the experiments it doesn't affect the conclusion.

The vortices trapped in the crystal are to be distinguished from the domain formation. We observed that for micron size crystals, all vortices exit when an external magnetic field is approaching zero because without external fields the Bean-Livingston and geometric barrier near edge don't allow enough room for a vortex to stay in the small size samples.

4.4. Measurements of Fluctuation

If the sample has a single chiral domain then, together, the chiral currents and the Meissner screening currents, would produce an additional magnetic moment along the c-axis with an order $\pm 1\times 10^{-12}$ e.m.u. However, to within the noise resolution of the experiment, the field-cooled magnetization curve of Figure 4.3 shows no signature of a zero-field moment, which limits its observed value to less than 2.5×10^{-15} e.m.u.

Several effects may account for this discrepancy: (i) a reduction of the edge currents [55], (ii) the presence of multiple domains [20], or (iii) insufficient thermalization of the particle during the field-cooling procedure. To resolve this discrepancy, a more systematic study is needed.

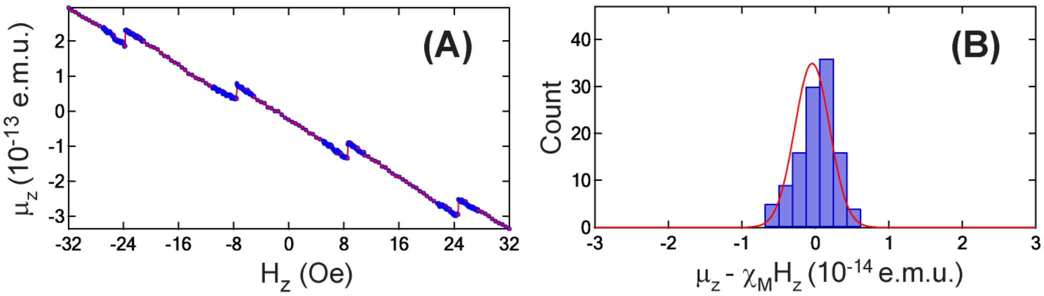

Figure 4.3 (**A**) Field-cooled data obtained at $T = 0.4\,\mathrm{K}$ for $H_x = 0$. To quantify the fluctuations in the magnetic moment μ_z, we subtract the Meissner response and histogram the difference $\mu_z - \chi_M H_z$. The histogram shown in (**B**) represent the fluctuations for field-cooled data between $-8\,\mathrm{O}e < H_z < 8\,\mathrm{Oe}$; the standard deviation fluctuations is $\sigma_z = 2.5\times10^{-15}$ e.m.u..

4.5. Vortex entry signatures

The time reversal symmetry ensures that dynamics involving the vortices with positive magnetic moments (pointing up) and ones with negative moments (pointing down) are equivalent. If the symmetry is broken, the asymmetry in the vortex entries depends on whether a magnetic field is swept from zero to positive fields or negative fields. A theoretical calculation for the time-reversal symmetry broken order parameter of UPt$_3$ was done by Tokuyasu et al. and it was shown that H_{c1}

differs up to 50% between a parallel and an anti-parallel magnetic fields to the angular momentum of the domain [56]. With the same argument applied to the chiral order parameter of Sr_2RuO_4, it is expected to observe several gauss of asymmetry in the vortex entry points. Figure 4.4 shows the magnetic field sweeps and corresponding vortex entries. The locations of the vortex entries are determined by the lower critical field of the crystal ($H_{c1} \sim 50\,\mathrm{G}$) and the specific sample geometry. The vortex entries at negative magnetic fields and positive fields are symmetric (there is a slight offset due to the earth magnetic field), and the change of the vortex entry points are less than ~0.2 G while three different field-cools were performed. This insensitivity of vortex dynamics to various field-cooling procedures was maintained throughout the whole series of experiments. Thus, we conclude that observations of the vortex entry signatures give consistent results with the measurement of fluctuation of magnetic moment in previous section, i.e. no observation of time-reversal symmetry breaking in these crystals.

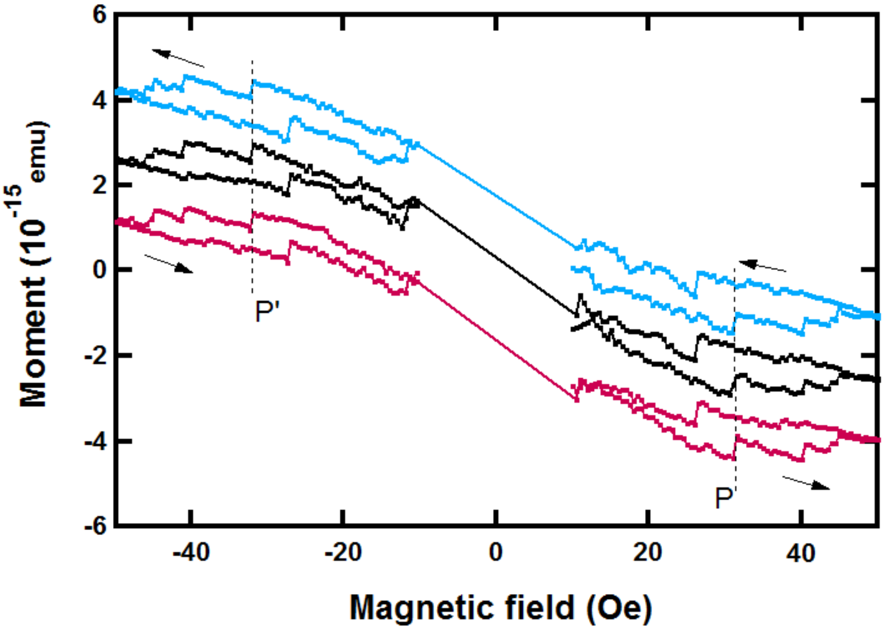

Figure 4.4 Signature of vortex entries. Three independent measurements after zero-field-cool were performed. Abrupt jumps in the magnetic moment represent vortex entries. P and P’ indicate points where first vortex enters the sample in positive and negative field, respectively, and those values are 31.3 Oe for P and -31.8 Oe for P’. The curves were translated vertically for better comparison.

4.6. Discussion

The observation of the chiral edge current will give evidence that the order parameter has broken time-reversal symmetry. The fact that we observe no evidence of it puts a significant constraint on the theoretical aspect of the chiral current mechanism and the possible order parameter scenarios of the crystal. On the other hand, if the theories about the spontaneous current and order parameter are correct, there are a few possibilities as follows. (i) The domain size should be considerably smaller than 1 μm. (ii) The domain walls move very easily in response to the external magnetic field, and thus the magnetic feature is practically indistinguishable from the conventional Meissner effect.

Alternative explanations also can be proposed [55]. One of those is that the surface effect of the sample, which induces a suppression of both p_x and p_y order parameter or emergence of different order parameter other than $p_x \pm ip_y$ at the edge of the crystal. Especially when a new order parameter, such as $p_x + p_y$, is developed near edge, the alternating current flows and the total magnetic moment can be much smaller than otherwise.

Other possibilities include multi-band effects and reduction of total angular momentum of superconducting condensate due to the effect of non-trivial band structure significantly different from the superfluid ^{3}He [57]. A number of measurements have shown evidence for a residual density of states at low temperature [5] and this is seemingly in contradiction with the fully gapped order parameter predicted above. This issue might be resolved by adapting scenarios such as horizontal line nodes and orbital dependent superconductivity (ODS) [58]; however, the fact that more complicated pictures are introduced signifies the possibility that Sr_2RuO_4 might not that analogous to the superfluid ^{3}He.

Another consideration arises when we remember the assumption/limitation of our measurement: there are small magnetic field present all the time. If the domain wall is so "soft" that it easily moves around even with sub-gauss magnetic fields, the magnetic signature will be temporally canceled out. On the other hand, Leggett proposed actual angular moment of the Cooper pairs to be $N\hbar(\frac{\Delta}{\epsilon})^2$ than what previously expected number $\frac{N\hbar}{2}$ [59]. However, the domain wall current would be also diminished, and it's puzzling to interpret the μSR experiments.

Chapter 5

Half-quantized fluxoid states in a mesoscopic ring

The half-quantum fluxoid state is a generalization of half-quantized vortex which confines flux of $\phi_0/2$. When magnetic fields penetrate deep into the bulk of the sample, the flux quantization condition needs to be generalized to the fluxoid quantization condition. The essential mechanism of π rotation of overall phase and $\mathbf{d}$-vector remains same, and the half-quantized fluxiod states have Majorana fermions in its core.

In this chapter we use cantilever magnetometry to measure the magnetic moment of micron-sized SRO rings, with the aim of distinguishing between half-quantized and full-quantized fluxiod states via changes in magnetic moment associated with the entry of single vortices. Half-height magnetic steps were observed in two samples with about ~1.5 μm diameter, and only full-quantized states existed in a larger sized sample of ~5 μm diameter. Data in this chapter have been published in [60].

5.1. Sample geometry and experimental conditions

We have fabricated annular samples by drilling a hole in the center of each particle using a focused ion beam. This geometry yields a discrete family of equilibrium states, in which the order parameter winds around the annulus as it would around a vortex core, but evades complications arising from the vortex core.

For a conventional annular superconductor, the fluxoid Φ', defined via $\Phi' = \Phi + (4\pi / c)\oint \lambda^2 \vec{j}_s \cdot d\vec{s} = n\Phi_0$, must be an integer multiple n of the flux quantum $\Phi_0 = hc/2e$ for any path encircling the hole (8). Here, $\vec{j}_s$ is the supercurrent density, $\Phi = \oint \vec{A} \cdot d\vec{s}$ is the magnetic flux enclosed by the path, $\vec{A}$ is the vector potential, and $n = \oint \vec{\nabla}\theta \cdot d\vec{s} / 2\pi$ is the order-parameter winding-number along the path. In the regime where the wall thickness of the annulus becomes comparable to or smaller than λ, $\vec{j}_s$ will not necessarily vanish in the interior of the annulus; hence, it is the fluxoid and not the flux that is quantized. The quantized winding of the order parameter, however, produces observable effects in the magnetic response of the annulus. In the regime in which the magnetization is piecewise linear in the magnetic field, the supercurrents that flow around the hole produce a magnetic moment $\mu_z = \Delta\mu_z n + \chi_M H_z$, where χ_M is the Meissner susceptibility and H_z is the component of the magnetic field that controls the flux through the hole. In equilibrium, changes in the fluxoid are associated with transitions in the winding number in single units (i.e., $n \to n+1$), corresponding to the changes in the magnetic moment in increments of $\Delta\mu_z$.

5.2. Estimation from Gibbs free energy

As Murakawa et al. suggested [61], it can be energetically favorable for $\mathbf{d}$-vector to lie on ab-plane of the crystal when a sufficiently large magnetic field along c-axis is applied. They suggested the c-axis field to rotate the d-vector less than 200G. In the case of $\mathbf{d}$-vector in ab-plane, a calculation of Chung et al. shows that half-quantum vortex is stable in mesoscopic size sample by spatially limiting divergent spin current energy [42].

Gibbs free energy per unit length of the vortex is given by

$$\frac{G\left(n_s, n_{sp}\right)}{\Phi_0 / 8\pi R^2} = \beta\left[\frac{1}{1+\beta}\left(n_s - \frac{\Phi}{\Phi_0}\right)^2 + \frac{\rho_{sp}}{\rho_s} n_{sp}^2\right] - \left(\frac{\Phi}{\Phi_0}\right)^2$$

, where $\beta = dR / 2\lambda^2$, $\Phi = \pi R^2 H$ and n_s, n_{sp} are vorticity of supercurrent and spin current respectively. Half-quantum stability comes when G(1/2,1/2) < G(1,0), which is the case if $\rho_{sp} / \rho_s < \left(1+\beta\right)^{-1}$. For He-3 ρ_{sp} / ρ_s was measure to be 0.3, and it is speculated that ρ_{sp} / ρ_s have similar value. Then, β of about 1~2 may stabilize the half-quantum vortices. Our small samples' dimension is in that range if you take account of elevated temperature at 0.5 K.

5.3. Observation of periodic fluxoid transitions

We start with the particle shown in Figure 5.1. In (**A**) The 80 μm × 3 μm × 100 nm single-crystal silicon cantilever has natural frequency ω₀/2π = 16 kHz, spring constant k = 3.6 × 10^{-4} N/m, and quality factor Q = 65,000, and exhibits a thermal-limited force sensitivity of $S_F^{1/2} \approx 1.0 \times 10^{-18}$ N/$\sqrt{Hz}$ at T = 0.5 K. Inset shows SEM image of the 1.5 μm × 1.8 μm × 0.35 μm annular SRO sample attached to the cantilever. The orientation of the *ab* planes is clearly visible from the layering observed near the edges of the SRO particle. Anisotropic component of the sus-susceptibility $\Delta\chi = \chi_c - \chi_{ab}$ as a function of temperature are shown in Figure 5.1(**B**). Here, χ_c and χ_{ab} are the *c*-axis and in-plane susceptibilities, respectively. Considering the bulk transition temperature, the T_c of this sample is diminished by 0.4 K. The decreased T_c can be understood by the small sized and damage done by FIB. Figure 5.1(**C**) Field-cooled data measured at T = 0.45 K for H_x = 0. To characterize its equilibrium fluxoid state, the particle is heat-cycled above T_c every data points in the presence of a static magnetic field H_z (i.e., field cooling). The field-cooled data (Figure 5.1) exhibits periodic steps in the magnetic moment, of nearly constant magnitude $\Delta\mu_z = (4.4 \pm 0.1)\times 10^{-14}$ e.m.u., period $\Delta H_z = (16.1 \pm 0.1)$ Oe, and susceptibility $\chi_M = -6.0\times 10^{-15}\,\mathrm{cm}^3$. The measured period ΔH_z matches ϕ_0 of flux threading a hollow superconducting cylinder having the dimensions of the sample [62,63]. Thus, we conclude that the periodic events observed in Figure 5.1(C) correspond to equilibrium transitions between *integer* fluxiod states of the annular Sr_2RuO_4 particle.

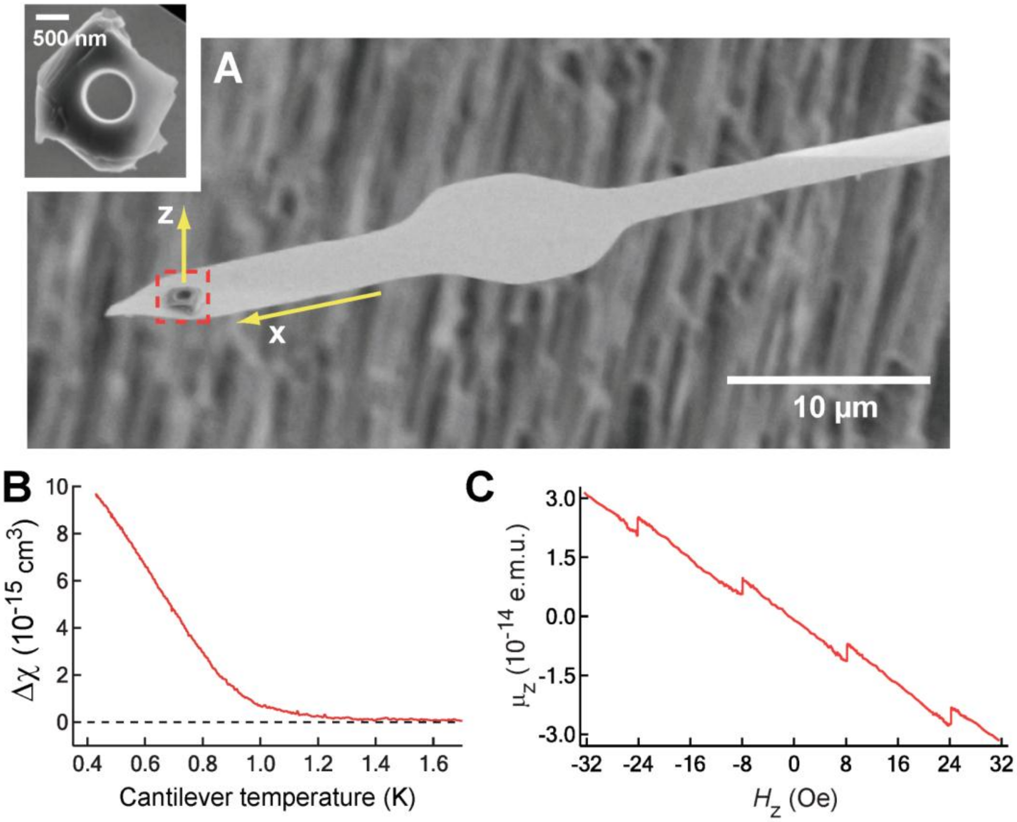

Figure 5.1 Image of cantilever with attached annular SRO particle.

5.4. Emergence of half-quantized fluxoid states

The presence of an in-plane magnetic field H_x brings two new features: (i) For $H_z = 0$, the in-plane magnetic response of the sample exhibits a Meissner behavior for $H_x < 250$ Oe. At $H_x = 250$ Oe, we observe a step in the in-plane magnetic moment with magnitude $\Delta\mu_x \approx 2 \times 10^{-14}$ e.m.u.; both the magnitude of the step and the value of H_x at which it occurs are consistent with those expected for the critical field $H_{c1} \parallel ab$ and $\Delta\mu_{ab}$ of an in-plane vortex for our micron-size sample. (ii) For $H_x < H_{c1} \parallel ab$, where no in-plane vortices are expected to penetrate the sample, and in the presence of H_z, we observe the appearance of half-integer (HI) states, for which the change in the magnetic moment of the particle is half that of the IF states.

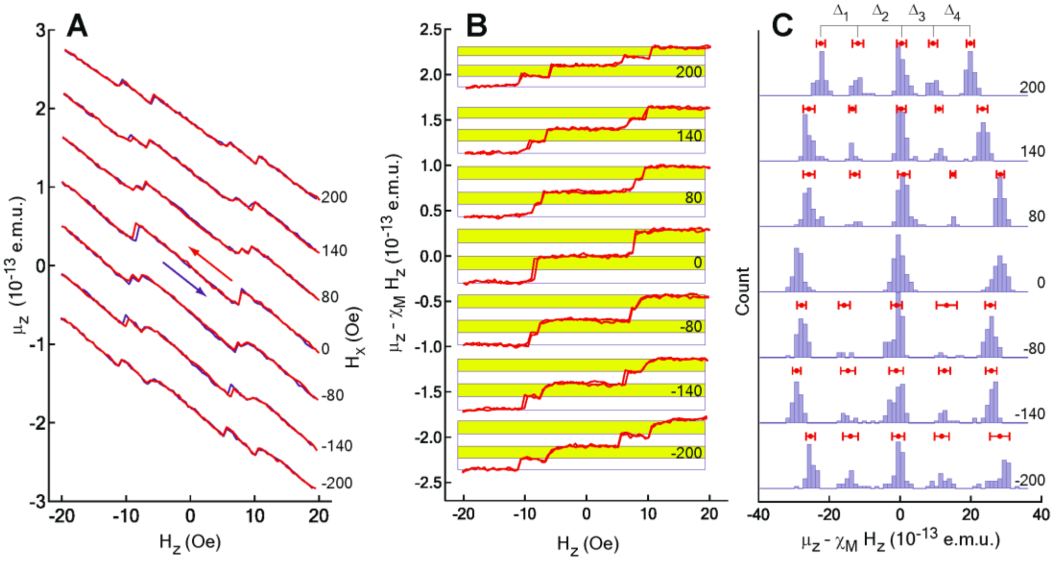

Figure 5.2 Evolution of the half-integer state with in-plane magnetic field.

Figure 5.2 (**A**) Zero-field-cooled data obtained at T = 0.6 K for in-plane fields H_x ranging from -200 to 200 Oe. The data were obtained by cooling the sample through T_c in zero field and performing a cyclic field sweep starting at H_z = 0 as arrows indicating. At this temperature, the zero-field cooled and field cooled data are nearly identical, indicating that the equilibrium response is well-described by the zero-field cooled data. In Figure 5.2 (**B**) data shown in (**A**) after subtracting the linear Meissner response; curves have been offset for clarity. Histogram of the Meissner-subtracted data are shown Figure 5.2 (**C**). The red points show the mean value of each cluster in the histogram, corresponding to the mean value of a given plateau; the horizontal error bars represent the standard deviation of a given cluster. The change in moment corresponding the i^{th} transition is labeled Δ_i. The steps clearly show that the change in magnetic moment is half of the transitions between two integer fluxoid states, indicating transitions between half integer fluxoid and full integer state.

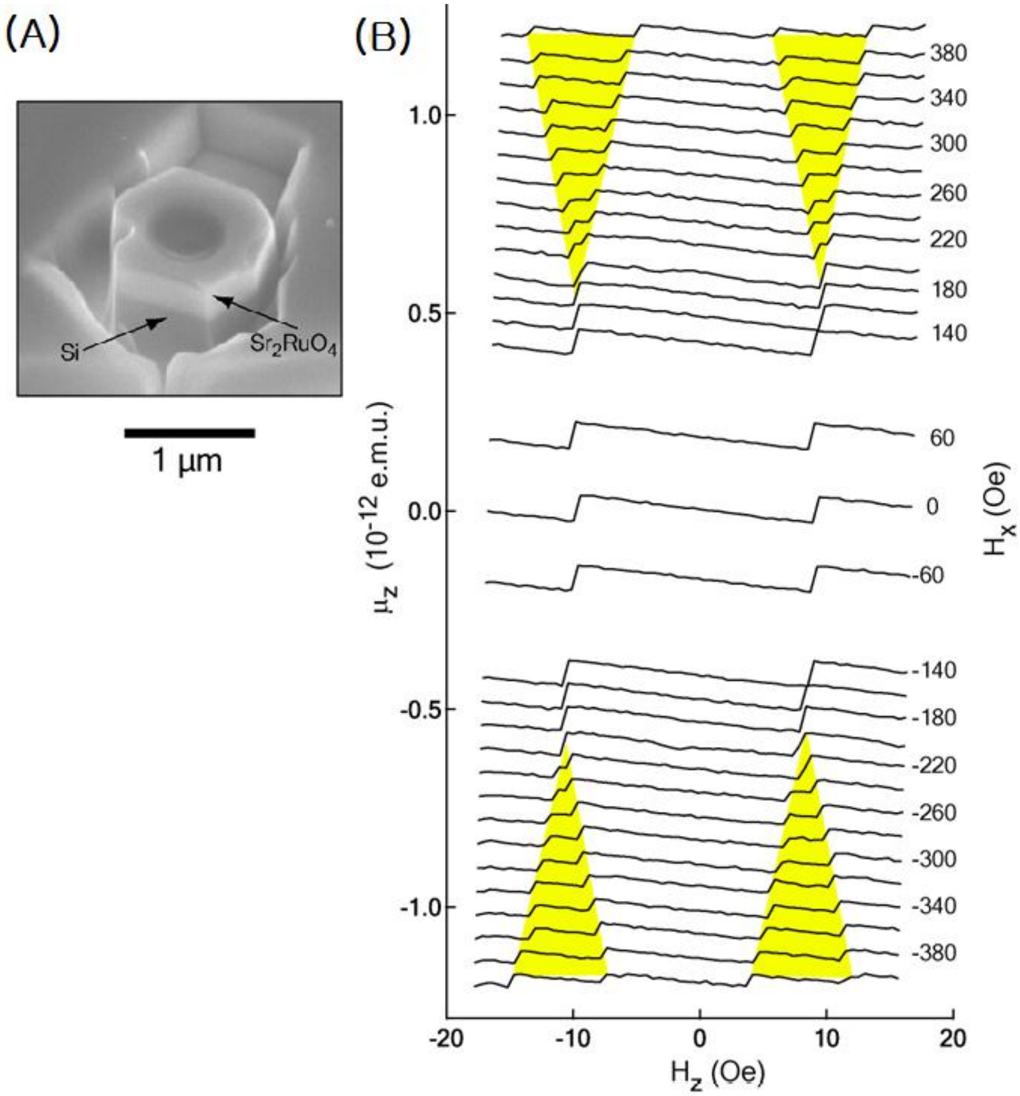

Figure 5.3 Plots showing zero-field-cooled data obtained at *T* = 0.5 K for the sample shown in (A)

The data shown in Figure 5.3 (B) represent the full magnetic response of the particle in (A). The yellow shading indicates the regions in which the half-integer state is stable. It's visually clear that one full transition becomes two half transitions.

These data contrast with the annular SRO samples whose dimensions are considerably larger than λ and a micron-size particle fabricated from $NbSe_2$, a spin-singlet, layered superconductor. For both of these samples, we find no corresponding half-integer transitions as the applied field is increased. A complicated set of fractional steps in the magnetic moment emerges; their fraction need not be one-half, and it changes with field. Furthermore, the pattern of fractional steps depends on the direction of the in-plane field (i.e., as $H_x \rightarrow -H_x$). The irregular pattern of fractional steps found for these particles is consistent with the presence of vortices in the bulk of the sample.

5.5. Robustness of half-quantized states

5.5.1. Invariance under magnetic field rotation

To investigate the dependence of the half-integer (HI) state on the direction of the in-plane magnetic field, we applied the in-plane magnetic field H_x along two directions rotated by 35 ° (see Figure 5.4). Our goal was to verify whether the direction H_x is important in the half-integer fraction observed in the magnetization steps accompanying fluxoid transitions as well as the dependence on the stability region of the HI state on the magnitude of the in-plane field. We find that the half-step features persist and, furthermore, that the field-dependence of the stability region is not strongly influenced by the direction of the in-plane field.

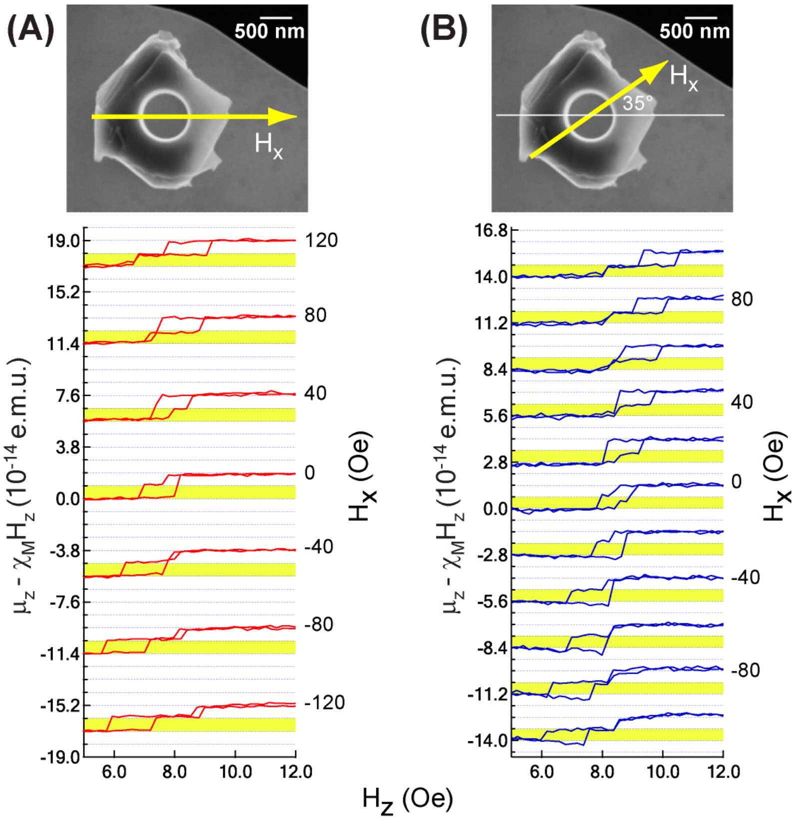

Figure 5.4. Stability of half-integer quantized fluxoids when the external field is rotated in ab-plane.

To vary the direction of H_x, the cantilever was mounted rotated in the xy-plane, yielding the data shown in Figure 5.4 (**B**). The data shown in Figure 5.4 (**A**) and (**B**) were obtained in separate experimental runs. To quantify clearly the change in moment associated with the observed transitions, we obtain χ_M by fitting to the linear Messiner response between $-8\text{Oe} < H_z < 8\text{Oe}$ for the $H_x = 0$ data and then subtract $\chi_M H_z$ from the data measured at different values of H_x.

5.5.2. Invariance under sample boundary change

To verify that the half step features we observe correspond to fluxoid states and not tilted or kinked vortex lines that pierce the sample walls, we performed a series of measurements on a particular SRO annulus to determine the dependence of the half-step states on the sample geometry. Prior to each of these measurements, we cut away more of the annulus, using the focused ion beam.

The motivation for this study was the following: the location and stability of a vortex line passing through the bulk of the sample should be sensitive to the sample geometry (e.g., the thickness of the walls of the annulus, or the location of pinning sites). By contrast, if the currents responsible for the half-step features are generated by a half-integer fluxoid, and thus only circulate the hole, the observed fractions should not be affected by the sample dimensions. Figure 5.5 shows measurements on a second SRO annulus; we again find that the in-plane magnetic field stabilizes a half-step state in which the observed fraction is very nearly a half (0.50 ± 0.02). Figure 5.5 (B) shows the image of the sample before shaping presented, as well as the outline after shaping (purple outline); after the cuts, the sample volume was reduced to 44% of the original volume, however the half-integer fraction was not affected (0.50 ± 0.01). We find that half-height step features observed in these samples are robust, and not sensitive to the wall thickness or the shape of the boundary, solidifying the conclusion the half-step features are the half-quantized fluxoids.

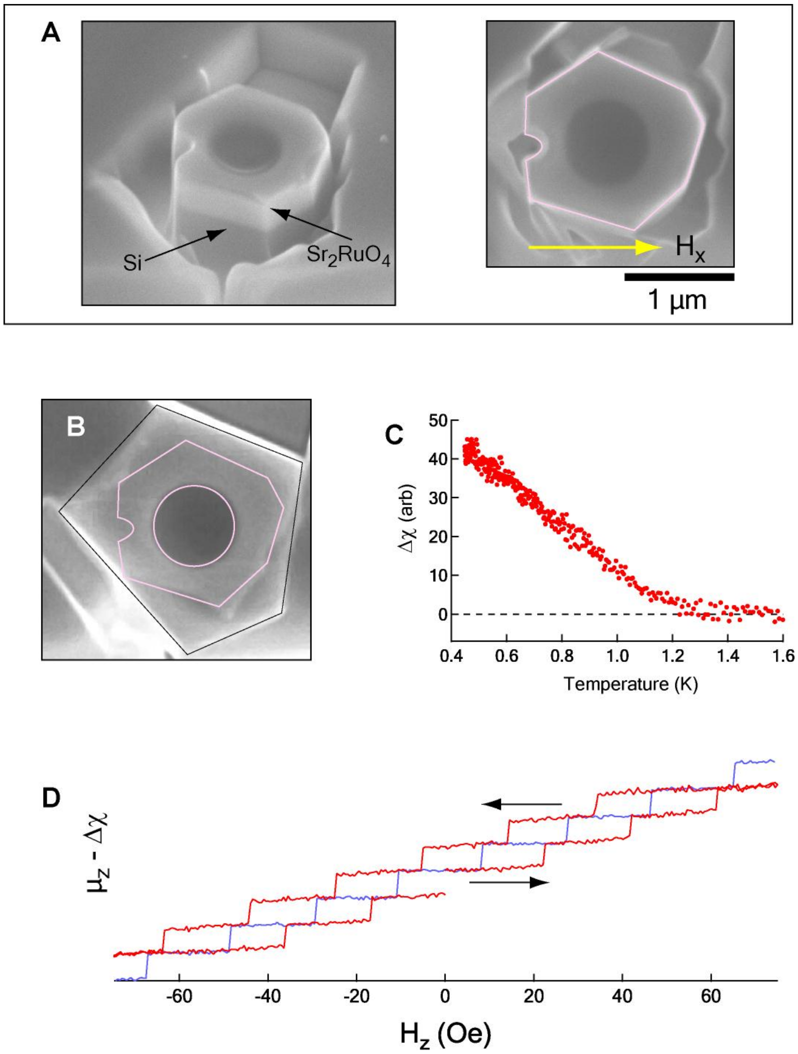

Figure 5.5 Reshaping the boundary of the sample.

5.6. Temperature dependence

The data were acquired at the value of the in-plane field indicated on the upper right-hand corner of each panel; all data were measured by field-cooling the samples. The Meissner response has been subtracted from all data; curves have been offset for clarity. In Figure 5.6 (**A**) data were obtained for the $NbSe_2$ sample. The data are scaled by: 4.5 K: 1.0×, 6.0 K: 1.7×, and 7.0 K: 10×. Figure 5.6 (**B**) shows the data obtained for the large SRO sample. The data are scaled by: 0.63 K: 1.0×, 0.72 K: 1.5×, 0.76 K: 2.3×, and 0.80 K: 6.0×. In (**C**) data were obtained for the SRO sample in Figure 5.1. The T = 0.55 K data is a plot of the c-axis moment acquired by applying the phase-locked modulation of δH_x = 1.0 Oe perpendicular to the c-axis. For the $T \geq 0.80$ K data, we measure $d\mu_z/dH_z$ by applying the phase-locked modulation (δH_z = 0.25 Oe) parallel to the c-axis. The magnetic moment curves are calculated by integrating the measured derivative signal.

The temperature dependence of the fractional steps measured for the large SRO (Figure 5.6A) and $NbSe_2$ (Figure 5.6B) samples show qualitatively different behavior than the half-step features observed for the smaller SRO sample, shown in Figure 5.1 (and Figure 5.6C). As the temperature approaches T_c, the fractional steps observed in Figure 5.6 (A) and (B) become less pronounced and most eventually disappear, leaving only the periodic fluxoid transitions. Numerical simulations for thin superconducting discs containing a circular hole find that as λ and the coherence length ξ become comparable to or larger than the wall thickness of the ring, the fluxiod states are favored energetically over bulk vortices (i.e., vortices penetrating the walls of the superconductor). Thus, at higher temperatures, bulk vortices should be less stable, in part because near T_c, ξ and λ will increase and eventually become large relative to the wall thickness and also because of increased thermal fluctuations. This behavior is consistent with the temperature dependence observed for the large Sr_2RuO_4 and $NbSe_2$ samples. In contrast, the HI transitions persist at higher temperature and the relative contribution to the magnetic moment from each half-step transition does not change significantly with temperature. Importantly, the half-step transitions measured for the SRO sample shown in Figure 5.1 exhibit a qualitatively similar temperature dependence to the fluxoid transitions; near T_c, the half-step transitions become reversible and broaden (Figure 5.6 C) indicating that ξ is comparable to the wall thickness in a portion of the ring. The HI transitions are clearly identified by the two double peaks in the derivative signal.

The half-integer states observed in magnetometry measurements performed on mesoscopic rings of SRO are consistent with the existence of half-quantum fluxoid states in this system. Our key findings—the reproducibility of the half-height steps in the *c*-axis magnetic moment in multiple samples and their evolution with the applied magnetic field demonstrates that the half-integer states are intrinsic to the small SRO annuli. These findings can be understood qualitatively on the basis of existing theoretical models of HQVs. In addition to the magnetic response, further studies will probe characteristics that are particular to the HQV state, such as spin currents or vortices obeying non-Abelian statistics .

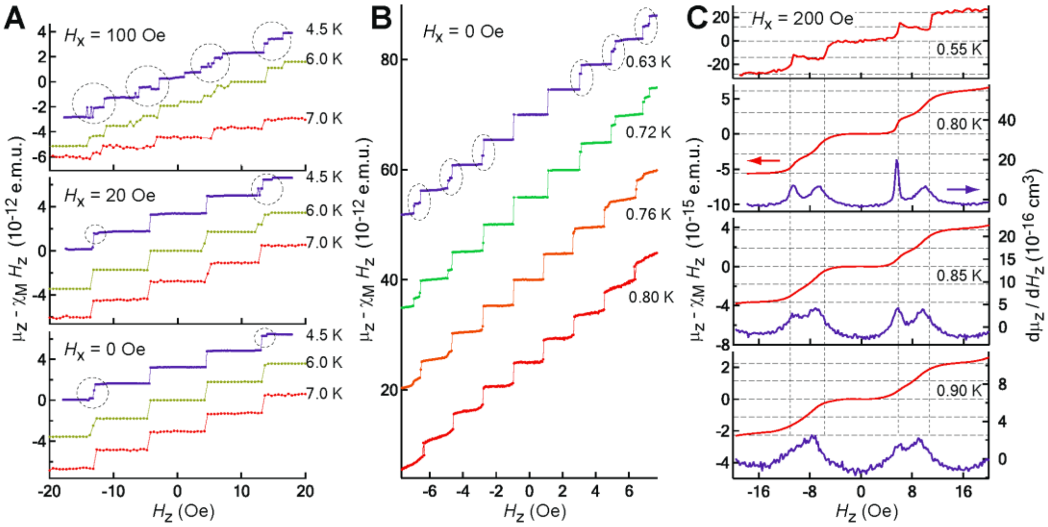

Figure 5.6 Temperature evolution of the fractional and HI states.

5.7. The kinematic spin polarization

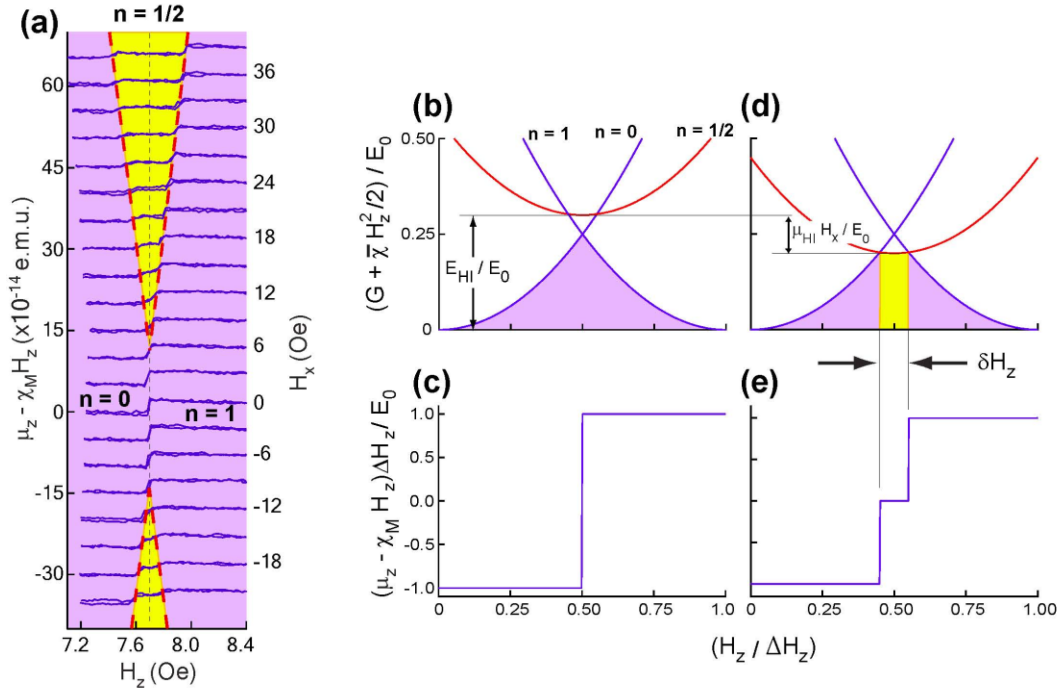

Figure 5.7 Stability of half-integer state with external in-plane fields.

If the steps represent transitions between half-quantized and full-quantized fluxoids, we expect the small steps are half size of full steps. The robust half-ness of the magnetization steps, which follows naturally from the theoretical framework of HQVs, is what we observe throughout the range of fields and temperatures studied. An analysis on the stability of the half-integer states necessitates an in-plane magnetic moment $\boldsymbol{\mu}_{\mathrm{HI}}$ only existing in the half-integer states. Then, the Gibbs free energy is written as

$$G(H,n) = E_0(n - H_z / H_z)^2 - \bar{\chi} H_z^2 / 2 + E_{\mathrm{HI}} - \mu_{\mathrm{HI}} H\,, \qquad (5.1)$$

where n can be integral or half-integral (i.e., half-integer states), and the parameters E_0 and $\bar{\chi}$ are expressible via measured quantities: $E_0 = \mu_z \Delta H_z / 2$ and $\bar{\chi} = \chi_{\mathrm{M}} + \mu_z / \Delta H_z$. Note that to account for the growth of the stability region of the half-integer states with in-plane magnetic field we have included two terms that are only nonzero in HI states: $-\mu_{\mathrm{HI}} H$, where $\boldsymbol{\mu}_{\mathrm{HI}}$ is a magnetic moment that exists only in the HI state and points in the direction of the in-plane field; and a field-independent constant contribution E_{HI}. We can relate the model parameters to the growth in the stability region of the HI state as a function of H_{x} : $\delta H_z = 4\mu_{\mathrm{HI}}(H_{\mathrm{x}} - H_{\mathrm{x,min}})/\mu_z$ (for $H_{\mathrm{x}} > H_{\mathrm{x,min}}$) and $E_{\mathrm{HI}} = E_0/4 + \mu_{\mathrm{HI}} H_{\mathrm{x,min}}$. For the particle of Figure 5.1, we find $E_0 \approx 0.1$ eV, $\mu_z \approx 2\times10^{-14}$ e.m.u., $\mu_{\mathrm{HI}} \approx 1\times10^{-16}$ e.m.u., and $E_{\mathrm{HI}}/E_0 \approx 0.26$. We note that the value of μ_{HI} obtained is roughly 200 times smaller than the magnitude of the magnetic moment measured for an in-plane vortex $\left(\Delta\mu_{\mathrm{x}} = 2.2\times10^{-14}\,\text{e.m.u.}\right)$.

While the origin of this moment is, as yet, unknown, recent work by Vakaryuk and Leggett [64] finds that a kinematic spin polarization $\boldsymbol{\mu}_{\mathrm{s}}^{\mathrm{kin}}$ can develop in the HQV state, as a result of the velocity mismatch between the $\left|\uparrow\uparrow\right\rangle$ and $\left|\downarrow\downarrow\right\rangle$ superfluid components. While, theoretically, the magnitude of $\boldsymbol{\mu}_{\mathrm{s}}^{\mathrm{kin}}$ depends on the distribution of both charge and spin currents, we estimate it to be of the same order of magnitude as the experimental value of $\mu_{\mathrm{HI}} \approx 1\times10^{-16}$ e.m.u..

To complete the interpretation of the experimental data, described by Figure 5.7, within the framework of HQVs, we consider two additional factors that are primarily responsible for the free-energy difference between the HF and IF states captured by the term E_{HI} in Eq. (5.1): one arises from the presence of spin currents; the other from spin-orbit interactions, which depend on the orientation of $\boldsymbol{d}$ with respect to the internal Cooper-pair angular momentum for the full and half quantum vortex states. The contribution from the spin currents is determined by their spatial distribution, and is proportional to the spin superfluid density ρ_{sp} [42,65]. To evaluate the contribution of spin-orbit interactions, both the orientation of $\boldsymbol{d}$ and the spin-orbit coupling strength are needed, which neither have been experimentally determined. Theoretically, there are several models for the order parameter of Sr_2RuO_4, which predict distinct orientations for $\boldsymbol{d}$ [5,66]. Our interpretation of $\boldsymbol{\mu}_{\mathrm{HI}}$ as being caused by a spin polarization implies that the ESP axis should be in the direction of the in-plane field for the range of fields studied. It is very important question how $\boldsymbol{d}$ -vector and the angular momentum of the pairs

The velocity mismatch between $\left|\uparrow\uparrow\right\rangle$ and $\left|\downarrow\downarrow\right\rangle$. spin components of an ESP superfluid in the HQV state gives rise to an effective Zeeman field B_{eff} which, in thermal equilibrium, produces a kinematic spin polarization in addition to that caused by the Zeeman coupling to the external field [64]. Such kinematic spin polarization is absent in the full-vortex state where the velocities of $\left|\uparrow\uparrow\right\rangle$ and $\left|\downarrow\downarrow\right\rangle$ components are the same, and generate an additional moment μ_{kin} in a direction to the external field in the half-quantized vortex state. The coupling between the kinematic spin polarization and the external field can account for the experimentally observed growth of the stability region of half-integer steps. The μ_{kin} is given by $\chi_s \int dv B_{eff} / V \sim \chi_s B_{eff}$,where χ_s is the spin susceptibility of Sr_2RuO_4, and

$$B_{eff}\left(r,H\right) = -\frac{m^*}{g_S \mu_B}\left(1+\frac{F_1}{3}+\frac{Z_1}{12}\right)\boldsymbol{v}_s\left(r,H\right)\boldsymbol{v}_{sp}\left(r\right).$$

Here, m^* is the Fermi-liquid mass of the charge carriers and g_S is their gyromagnetic ratio. Fermi-liquid parameters F_1 and Z_1 describe renormalization of charge and spin currents respectively; $\boldsymbol{v}_s$ and $\boldsymbol{v}_{sp}$ are the local charge and spin superfluid velocities respectively; the superfluid velocity v_s which describes motion of charges in the system couples to the applied field $\boldsymbol{H}$. Using the estimates for $B_{eff} \sim 5\,\mathrm{G}$ and $\chi_S \approx 1\times10^{-17}\mathrm{cm}^3$, which is obtained from the molar spin susceptibility of Sr_2RuO_4 (i.e. 10^{-3} e.m.u./mol [67]), we find and $\mu_S^{kin} \approx 10^{-16}\text{e.m.u.}$, in agreement with the experimentally observed value.

5.8. Other possible scenarios for the HI state

We discuss other possible scenarios for the theoretical interpretation of the half-integer state. Namely, π-junction scenario and "wall vortex" scenario. We show that the two scenarios are not consistent with our observations.

5.8.1. The π-junction scenario

Under certain circumstances, there can exist crystal grain boundary Josephson junctions within the sample that can shift the total phase winding by π [68]. However, our samples are fabricated from high quality single crystals, and thus it is unlikely that they contain the grain boundaries and orientations necessary to realize a π-junction. Moreover, even assuming that the presence of a π-junction, its will shift the values of the out-of-plane magnetic field at which the fluxoid transitions occur by $\Delta H_z / 2$. We do not find evidence of such a shift in our data. Furthermore, the π-junction scenario would produce jumps in magnetic moment identical to that for a conventional full-quantum vortex. It would not lead to the half-height jumps of the magnetic moment. Therefore, it doesn't seem that such a scenario is relevant to our observations.

5.8.2. The wall vortex scenario

We refer to a wall vortex as any state where a vortex penetrates through the volume of the sample. In general, a transition between a state and the $n = 0$ integer fluxoid state will correspond to a change in the particle's magnetic moment μ_{WV}. Thus, to interpret the HI state as a wall-vortex state, μ_{WV} would need to be consistent with the observed value of $(\mu_z/2)\hat{z}+\mu_{HI}$. For the experimental particles where the HI state is observed, the local superconducting properties are not known in detail. Therefore it is difficult to constrain the possible forms of wall-vortex states. However, we can make the following general observations: (i) For the observed in-plane vortices corresponding to fields $H_x \geq 250\,\mathrm{Oe}$ (Fig. S3), the magnitude of the in-plane component of μ_{WV} is approximately 200 times larger than μ_{HI}. Thus, the HI state is not a simple generalization of the observed in-plane wall-vortex state. (ii) The z-axis component of μ_{WV} can be any fraction of μ_z and is not generically $\mu_z/2$. (iii) In general, we would expect the location/orientation of wall vortices to vary with the magnitude and direction of the applied field. Hence, generally we expect multiple fractional steps in the magnetic moment; these steps correspond to transitions involving various configurations of wall-vortex states. (iv) Given the geometric asymmetry of our samples, we would also expect that the component of $\Delta\boldsymbol{\mu}_{WV}$ along the in-plane field to vary with the direction of the in-plane field. Consequently, the stability region of the wall-vortex state should be affected by the direction of the in-plane field. However, over the range of fields studied for the Sr_2RuO_4 particle shown in Figure 5.4, we find that the stability region and relative magnitude of the half-integer feature is not changed by the direction of the in-plane field. Given these considerations we conclude that to formulate a wall vortex scenario consistent with the observed properties of the half-integer state would require a fine tuned set of assumptions, and is thus unlikely.

5.9. Discussion of the results

Based on our observations, a half-quantized vortex or fluxoid is likely stabilized in a micron-size spin-triplet p-wave superconductor. Still, the decisive experiments would be a measurement of spin dynamics associated with the $\mathbf{d}$-vector winding. In the presence of the half-quantized vortices, one can utilize Josephson interferometry, which is sensitive to the orientation of the $\mathbf{d}$-vector to junction interfaces [53,54] and spin-dependent tunneling spectroscopy [69,70] with spatial resolution to search for existence of the spin velocity. The investigation of Josephson effect through a weak-link junction might also reveal exotic spin dynamics signature, given our current geometry of the sample and a sensitive magnetometry setup. In Chapter 6, the measurement of current-phase relationship in a weak-link junction will be presented.

Another exciting phenomenon closely related to the half-quantized vortex is the existence of Majorana fermion. Motivated by the proposal to implement a decoherence-free quantum computation, recent advances in the research activities on the topological phases and Majorana fermion become a big motivation to our experiment. In next section we will discuss the relevance of the observed half-quantized fluxoid states to the exotic excitations in the topological superconductors.

5.10. Majorana fermion

The Majorana Fermion is the zero-energy quasiparticle state near the vortex core and has a property of having identical creation and annihilation operators. Ivanov showed[71] that the quasiparticles satisfy the non-commutative exchange operation, or non-Abelian statistics. Very similar property of quasiparticle at filling factor of $\nu = 5/2$ FQHE was studied by Moore and Green, and later proposed as a candidate for the topological quantum computation. The fact that the state is topologically protected with the globally defined excitation gap, makes the quasiparticles resistant to local decoherence.

The important point is that the triplet condensate has an additional spin degree of freedom. The spin degree of freedom is represented by the d-vector formalism, which is well known in literatures about He-3 superfluid. The order parameter, band gap and wave function are expressed with the d-vector formalism accordingly. In a bit simplified case, if the d-vector is confined on a plane, which is likely situation in real world, then we can define Fixed Equal Spin Pairing axis to the axis of rotation, and the wave function is represented by up and down spin component in the direction. It is also readily apparent that the relative phase winding between the up and down spins will involve a rotation of the d-vector and gives spin current. And coherence of overall phase will generate charge current.

5.10.1. Brief introduction

Exotic quasiparticles in a spin polarized fractional quantum Hall liquid (for example $\nu = 5/2$ state) were studied by the Moore and Read [72], and it was realized that the quasiparticles are Majorana fermions, whose creation and annihilation operators are identical to each other, and satisfies non-Abelian braiding statistics. Later Read and Green found out that excitations in vortex cores of spinless $p_x \pm ip_y$ superconductor have the same topological properties [40]. The non-Abelian braiding statistics is in the heart of the recently proposed topological quantum computation [41] and the fact that the state is topologically protected, with the globally defined excitation gap, makes the quasiparticles resistant to local decoherence [73].

If Sr_2RuO_4 is found to be the 2-dimentional spinful $p_x + ip_y$ superconductor, it is expected to have a zero-energy Majorana bound state in the core of its half-quantum vortex (HQV). The HQV is considered as a full quantum vortex of only one spin component, leaving the other spin component without a vortex. Consequently, the separable Bogoliubov-de Gennes equation for “up”-spin and “down”-spin components render a HQV the physical equivalence to a vortex in the spinless $p_x \pm ip_y$ superconductors, therefore realizing Majorana fermions. The zero-energy mode is protected by particle-hole symmetry of a superconductor: a non-degenerate single Majorana state cannot have non-zero energy because by the particle-hole symmetry it requires another degree of freedom to have opposite energy. In a same logic, two Majorana fermions in close proximity are equivalent to no Majorana fermion, i.e. it’s no more protected. Interestingly, the even dimensionality of BdG equation requires a counterpart of a Majorana fermion in a vortex core. When a single vortex exists in a finite sample, the other Majorana mode, thus, will be at the edge of the sample. Thus, robust quantum computation with Majorana fermions will requires good separation between vortices and from the edge.

5.10.2. Majorana fermion in half-quantized fluxiod state

An important question is if the Majorana bound state is still present in the annulus Sr_2RuO_4 sample when the half-quantized fluxoid states are stable. Given the half-quantized vortex is considered as a full vortex of one spin component and no vortex for the other, a hole in the sample will only affect the component with a vortex and has an effect of extending the vortex core area. The topological property to require the existence the zero mode changes only when the bulk superconducting gap is closed. Imagining that the core area of a vortex is adiabatically increased, the bulk gap in the bulk of the superconductor is maintained non-zero. The Majorana fermion in the vortex core before the modification will be protected throughout the process. Shortly speaking, considering the topological reason a Majorana fermion exists within the core of a vortex of the spinless $p_x + ip_y$ superconductor, the Majorana fermion and the topological phase boundary may exist in the *inner surface* of the hole in the sample. Note that Sau and collaborators solved an analytical solution for the Majorana zero mode in a heterostructure topological superconductor with annular geometry. They assumed that the energy gap become zero in the hole and constant magnitude in the bulk.

The zero energy mode is energetically separated from the next excited states by $\delta_0 \sim v_F / k_F \xi^2 \sim \Delta^2 / \epsilon_F \sim 1\,\mathrm{mK}$ [74]. To operate as a topological qubit, the energy splitting should be more than the thermal energy, which requires $k_B T << \Delta^2 / \epsilon_F$. When the core is replaced with a hole, ξ in the expression for the energy splitting should be replaced with the circumference of the hole. This makes the splitting about an order smaller and thus results in the temperature requirement prohibitive to about $100\,\mu\mathrm{K}$. For additional consequences of having the current geometry of the sample, further theoretical studies are necessary.

Another non-ideal effect is possibly caused by the 3-dimensionality of the crystal. So far in the discussion of the Majorana fermion, we assumed that strictly 2-dimensional layers independent each other, thus having its own the zero-mode state. There are hundreds of unit layers in the SRO crystal in the experiment, and there will be hundreds of Majorana fermions in the core of a half-quantized vortex. The question to be addressed is whether the Majorana fermions will interact with each other, energy splitting occurs, and the zero energy states are no more protected. Currently, it issue seems to be an open question.

Chapter 6

Weak-link junctions

As a way to study spin-triplet p-wave superconductors, Josephson tunneling effects between s-wave and Sr_2RuO_4 played an important role. However, attempts to fabricate high quality Josephson junctions present technical difficulties: high-quality superconducting SRO samples are synthesized not as thin films but as bulk crystals, and conventional photolithography cannot be used for the fabrication of tunneling junctions. Also, scanning tunneling spectroscopy experiments found that the surface of the p-wave 1.5 K phase is very fragile [16].

We take a slightly different route: this chapter is about fabrication of a weak-link on a Sr_2RuO_4 superconducting ring and the observation of anomalous second harmonic component in the current vs. applied flux, which can be interpreted as originating from the charge and spin degree of freedom of the order parameter of Sr_2RuO_4.

6.1. Geometry of the samples and measurement

The challenge we face in preparing sample comes from the fact that Sr_2RuO_4 is a low-temperature unconventional superconductor with a fairly long coherence length: non-magnetic defect easily suppress superconductivity. Sr_2RuO_4 cannot be deposited in the form of film with high transition temperature, making it very hard to use usual nanofabrication techniques. Thus, we had to work directly with the bulk single crystals grown by the floating zone method.

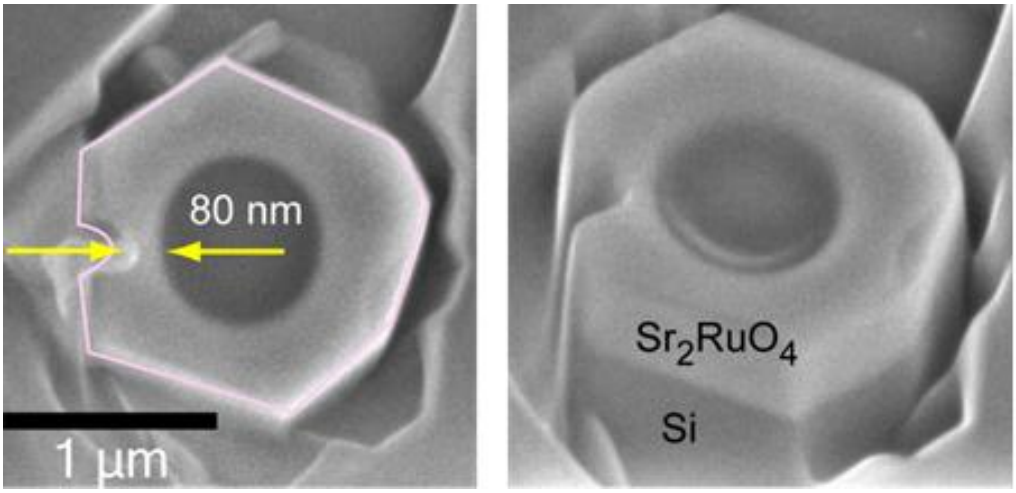

Figure 6.1 SRO crystal and a weak-link.

We start from a micron size annulus sample used in the half-quantized fluxiod experiments. A hole and a constriction were milled using 30 keV Ga ion Focused Ion Beam (FEI DB235) with a few pico-amps of current to minimize the sample damage. The size of constriction needs to be comparable to the coherence length of the superconductor, about 70 nm at zero temperature. Because the resolution of the Focused Ion Beam is about 30 nm, the fabrication of ~ 70 nm constriction needs a careful management of location and milling time to get desired weak-links. If the milling is done only from the top view, i.e. parallel to c-axis of the crystal, the weak-link becomes Dayem bridge [75], which is basically of small size in in-plane dimensions but having a height of original crystal. The primary data presented in this chapter is from weak-links of fabricated by milling only parallel to the c-axis.

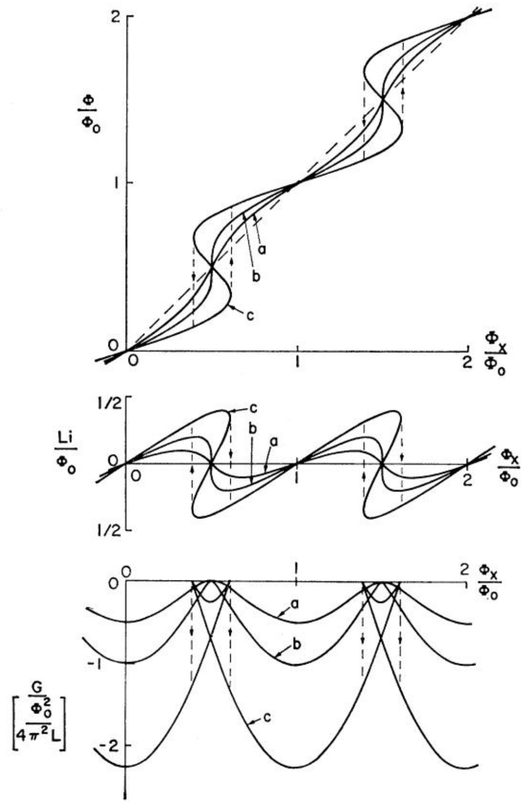

Figure 6.2 Characterization of weak-link junction. Total magnetic field, current in the ring, and Gibbs free energy is shown each panel. As the critical current of the junction decrease, phase-slip transitions become smoother. From [76].

The current response of a superconducting ring with a weak-link was studied by Silver and Zimmerman, who invented Superconducting Quantum Interference Device in 1960's [76]. In Figure 6.2, y-axis is total flux inside a ring and x-axis is applied field. After subtracting the linear Meissner response, one obtains the circulating current which varies periodically with the applied flux. The response of the annulus sample is well described by the periodic phase-slips when external field is swept, and the periodicity is the flux quantum divided by the effective area. The transition becomes continuous and non-hysteretic when the junction starts to become a weak-link and the critical current of the junction is significantly suppressed. By using the load line equation $\Phi + Li = \Phi_x$, fluxiod quantization condition, and sinusoidal current-phase relationship, one can deduce following relations:

$$\Phi + Li_c \sin(2e/\hbar)(\Phi - k\Phi_0) = \Phi_x \tag{6.1}$$

$$Li = -Li_c \sin(2e/\hbar)(Li + \Phi_x - k\Phi_0)\,.$$

Here, Φ_x is the external flux parallel to the loop axis; i_c and L are the critical current of the junction and the inductance of the loop. Figure 6.2 was plotted based on Eq. (6.1). While limited by assuming sinusoidal current-phase relationship, it is a good starting point to understand the qualitative features of the response of weak-links. With this guidelines, junctions of about 100nm ~150nm were fabricated; however, the current response showed strong hysteretic behaviors indicating the critical current of the junction is not small enough, i.e. $i_c L/\phi_0 \ll 1$. After successive FIB cuts, the junction dimension was reduced to 80nm; the transition become non-hysteretic and exhibited a skewed sinusoidal behavior. The emergence of the smooth transitions in terms of the weak-link size is fairly abrupt, indicating discrepancy of the apparent link size and the undamaged effective one.

6.2. Appearance of second harmonics

6.2.1. Gibbs free energy analysis

When the out-of-plane magnetic field (denoted as H_z) is swept with the zero in-plane magnetic field (denoted as H_x), the current response is skewed sinusoidal which resembles s-wave superconducting weak-link junctions. However, when a non-zero in-plane magnetic field is applied, it starts to give anomalous magnetic responses (see Figure 6.3). The χ, which is derivative of the magnetic moment to fields, shows clearer picture that it develops a second harmonic component. Also, note that the distance between two peaks grows with in-plane fields, reminiscent of the half-steps in Chapter 5.

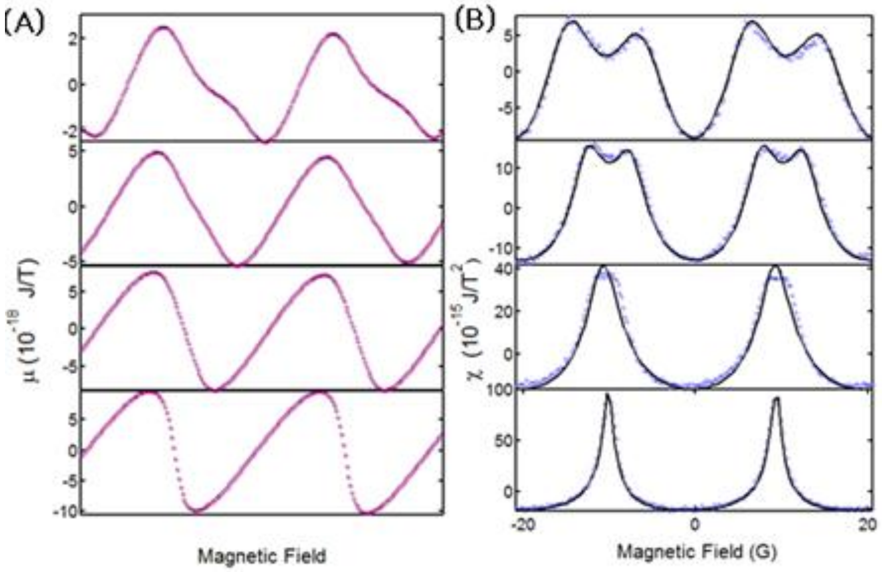

Figure 6.3 Appearance of second harmonics. (A) and (B) are showing magnetic moments and susceptibility in functions of applied magnetic fields. Columns from top to bottom in each graph represent 900G, 700G, 500G, and 300G in-plane fields.

To understand the underlying mechanism, we setup a simple model for spin-triplet weak-link (See Figure 6.4). The analysis is as follows. In the thick junction limit, i.e. a ring without a weak-link, Gibbs free energy is expressed as

$$G(n)=\frac{\Phi_0^2}{2L}\left(n-\frac{\Phi_a}{\Phi_0}\right)^2,$$

where, n is an integer representing a vorticity, which realizes discrete phase slips. Then, if you imagine a spin-singlet weak-link junction in a ring, and assume that the junction is in an ideal Josephson coupling limit. The Gibbs free energy can be written in terms of the phase difference developed across the junction, and it can be shown that the current and phase has a sinusoidal relationship. Above equation can be modified to account the continuous phase across the junction as

$$G(\theta)=\frac{\Phi_0^2}{2L}\left(\frac{\theta}{2\pi}-\frac{\Phi_a}{\Phi_0}\right)^2-E_J\cos\theta,$$

where, $E_J=\phi_0 I_c/2\pi$.

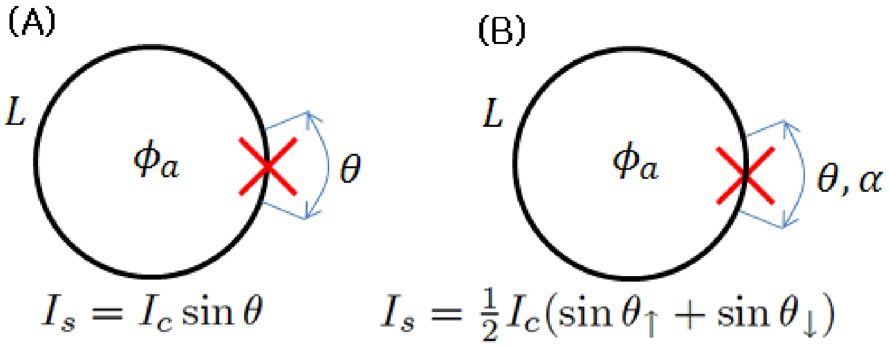

Figure 6.4 Current phase relationship derived from Gibbs free energy functional

In contrast to the spin singlet case, for a spin triplet superconductor, you should consider two different components for each spin.

$$G(n)=\frac{\Phi_0^2}{2L}\left[\left(n_s-\frac{\Phi_a}{\Phi_0}\right)^2+\gamma n_{sp}^2\right],$$

where n_s and n_{sp} are charge and spin vorticity, respectively. When a junction become weak-link, we define θ and α, charge phase and spin phase difference across the junction, respectively, then the Gibbs free energy becomes

$$G(\theta,\alpha)=\frac{\Phi_0^2}{2L}\left[\left(\frac{\theta}{2\pi}-\frac{\Phi_a}{\Phi_0}\right)^2+\gamma\left(\frac{\alpha}{2\pi}\right)^2\right]-(E_J/2)\cos\theta_\uparrow-(E_J/2)\cos\theta_\downarrow$$

$$(E_J/2)\cos\theta_\uparrow+(E_J/2)\cos\theta_\downarrow=E_J\cos\theta\cos\alpha$$

$$G(\theta,\alpha)=\frac{\Phi_0^2}{2L}\left[\left(\frac{\theta}{2\pi}-\frac{\Phi_a}{\Phi_0}\right)^2+\gamma\left(\frac{\alpha}{2\pi}\right)^2\right]-E_J\cos\theta\cos\alpha, \qquad (6.2)$$

where, $\gamma = (1+\beta)\rho_{sp} / \rho_s$, $\theta = (1/2)(\theta_\uparrow + \theta_\downarrow)$ and $\alpha = (1/2)(\theta_\uparrow - \theta_\downarrow)$. In order to explain the increased second harmonics with higher in-plane magnetic fields, it still needs an additional term in the Gibbs energy and we will discuss possible mechanisms in the following sections.

6.2.2. Role of in-plane magnetic field: possible scenarios

1) Kinematic spin polarization

The kinematic spin polarization mechanism in Chapter 5 can explain the role of the in-plane field by introducing an additional term $\mu_{HI} H_x |\alpha| = b|\alpha|$ to the Gibbs energy (6.2) as

$$G(\theta,\alpha) = \frac{\Phi_0^2}{2L}\left[\left(\frac{\theta}{2\pi} - \frac{\Phi_a}{\Phi_0}\right)^2 + \gamma\left(\frac{\alpha}{2\pi}\right)^2\right] - E_J \cos\theta \cos\alpha - b|\alpha|.$$

Now, we can derive the functional form of the spin-triplet current response using the variational method. From the stationary conditions $\partial G / \theta = 0$ and $\partial G / \alpha = 0$,

$$\phi_z = \phi + \frac{\phi_0 E_J}{4\pi E_0} \sin\theta \cos\alpha$$

$$2E_0 \gamma\alpha + E_J \cos\theta \sin\alpha - b = 0.$$

The current has the relationship with these two phases following

$$I_s = I_c \sin\theta \cos\alpha .$$

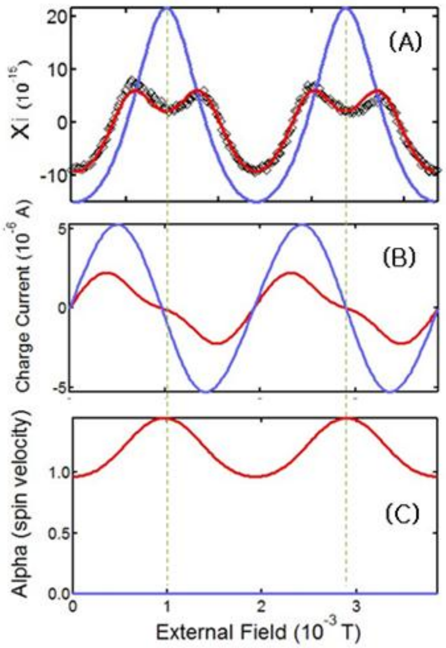

Figure 6.5 (A) Susceptibility, (B) charge and (C) spin current fitted by the equations based on the kinematic spin polarization term. An in-plane field of 900 G is applied. Red curves are fitted with both charge and spin degree of freedom, and blue curves are fitted with only charge contribution.

Figure 6.5 shows the fit of experimental data using the relations. The blue curves are fit curves based on the singlet model and the red curves are based on the triplet model. The data in Figure 6.5 (C) show α as the results of the fit, and it explains the qualitative feature of the second harmonics: when the spin phase is plotted against external fields, it peaks around $\phi_0 / 2$ point, and it can be seen as an energy saving mechanism by flowing spin current under the kinematic spin polarization energy gain. We, however, emphasize that the spin current shown in the Figure 6.5 (C) might be unphysical results because it has always positive value, which might be resolved in the next scenario.

2) Induced misoriention of $\mathbf{d}$-vector across junction

The appearance of the second harmonic components can be explained when dynamics of $\mathbf{d}$-vector is involved. Rashedi et al. studied triplet superconductor-normal metal-triplet superconductor (TS-N-TS) junctions, and calculated the current-phase relationship using the quasiclassical Eilenberger equation [77]. The results showed that the difference of $\mathbf{d}$-vector orientation across the junction induces spin currents and thus second harmonics in the current phase relation. If the in-plane magnetic field H_x are interacting with the $\mathbf{d}$-vector to be mis-oriented across the junction, then the up-spin and down-spin phase is modified to $\theta_\uparrow \to \theta_\uparrow + \alpha_0(H_x)$, $\theta_\downarrow \to \theta_\downarrow - \alpha_0(H_x)$. Therefore, Gibbs free energy is given by

$$G(\theta,\alpha) = \frac{\Phi_0^2}{2L}\left[\left(\frac{\theta}{2\pi} - \frac{\Phi_a}{\Phi_0}\right)^2 + \gamma\left(\frac{\alpha}{2\pi}\right)^2\right] - E_J \cos\theta \cos(\alpha - \alpha_0(H_x)).$$

The same variational method gives

$$\phi_z = \phi + \frac{\phi_0 E_J}{4\pi E_0} \sin\theta \cos(\alpha - \alpha_0)$$

$$2E_0\gamma\alpha + E_J \cos\theta \sin(\alpha - \alpha_0) = 0 .$$

In Figure 6.6 the fitted susceptibility curves are plotted with resulted charge and spin current. It should be noted that spin current in (C) is oscillating around zero, which is different from the kinematic spin polarization analysis.

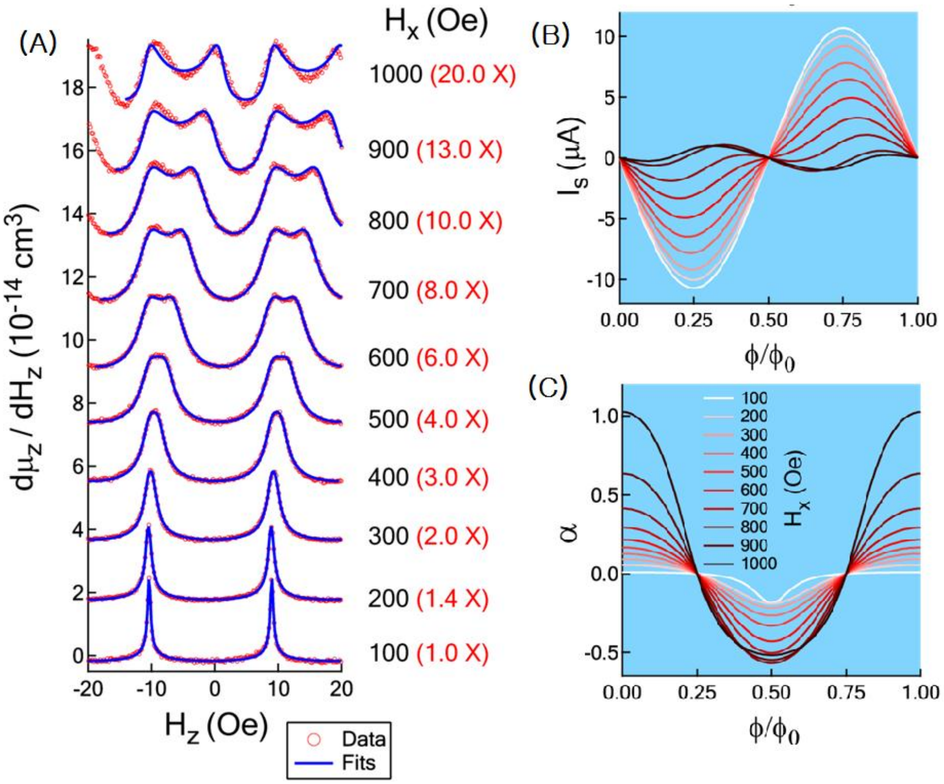

Figure 6.6 (A) Susceptibility, (B) charge and (C) spin current fitted by the equations based on the picture of misoriented $\mathbf{d}$-vector across the junction. In this case, spin current in (C) is oscillating around zero, which is different from the kinematic spin polarization analysis.

6.2.3. Remarks on experimental limitation

To reveal the whole picture of the current phase relationship, one should be able to change the theta and alpha independently. In this experiment, however, the fact that the junction is involved in a ring constrains θ and α. Given the limitation, our data are consistent with the spin dynamics in a spin-triplet superconducting junctions.

To make the dimension of a weak-link smaller than the coherence length in all 3-dimensions, FIB milling was performed angled 52 degree to c-axis. Second harmonic feature didn’t appear up to 1000G of in-plane fields, suggesting the weakened Josephson coupling and the second harmonic component becoming less energetically favorable. The weakened coupling across the junction may suppress the involvement of spin degree of freedom. Controlled experimentation with junctions of different shape and size are needed.

6.2.4. Temperature dependence

Figure 6.7 shows temperature dependence of the second harmonics which tend to disappear at high temperatures. The temperature dependence can be understood by considering the temperature dependence of γ term in Eq. (6.2). The γ term is proportional to ρ_{sp} / ρ_s, the spin fluid density over charge superfluid density, which is known to increase to 1 as temperature raised close to T_c in superfluid ^{3}He. If we assume that the qualitative behavior remains same in triplet superconductors, although not much is known about the case, then it becomes energetically more costly to flow spin current at higher temperature; thus, the second harmonics fade away.

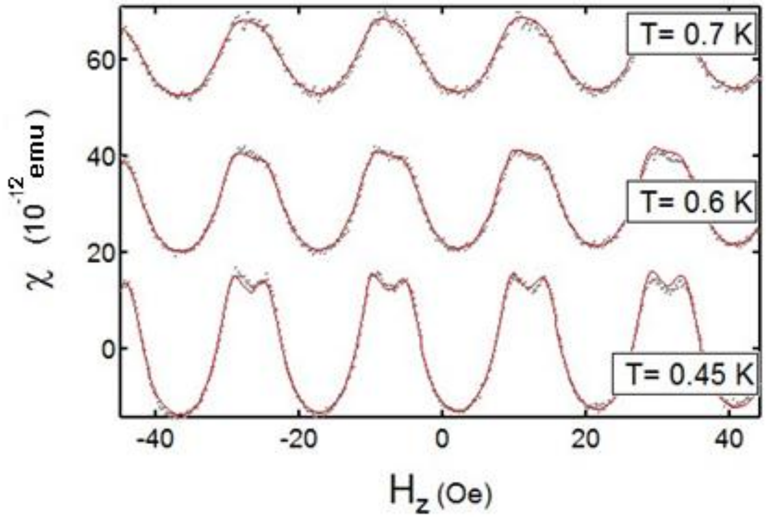

Figure 6.7 Temperature dependence of the second harmonic component.

6.3. Discussion and outlook

Similar phenomena were observed in the Josephson effect experiment in superfluid ^{3}He. The flow of superfluid ^{3}He-B through a 65x65 array of nanometer size apertures has been measured by Backhaus et al at Berkeley [78,79]. They found a new branch, so-called π state, in the current-phase relation. The π state has subsequently been observed also in a single narrow slit and the transitions into and out of π state become smooth, showing qualitatively similar behavior.

In order to explain the π state, Viljas et al. performed calculations in two limiting cases [80]. The first case is one large aperture, where the 18-component order parameter is solved numerically in and around the aperture using the Ginzburg-Landau theory of ^{3}He. The current-phase relationship shows the existence of the π state for sufficiently large apertures. Their interpretation is that the π state corresponds to a phase slip by a half-quantum vortex. The π state corresponds to the case of equal spin-orbit rotation matrices on the two sides of the weak link. Calculations for an aperture that is small compared to the superfluid coherence length were performed by Yip using a simplified model [81]. It was found that π state occurs in a single pinhole only at low temperatures, a feature qualitatively similar to our result, thus giving hints to our experiments given the similarity of Sr_2RuO_4 and superfluid ^{3}He.

The experiments and calculations are done with ^{3}He-B and the Sr_2RuO_4 is more analogous to ^{3}He-A; however, the combined dynamics of orbital and spin degree of freedom in ^{3}He-B experiments are very suggestive to how the complicated structures like second harmonics show up in current response of Sr_2RuO_4 weak-link junctions. While appropriate Gibbs free energy constructions could qualitatively explain the observed second harmonic phenomenon, and suggests the exotic spin and charge current dynamics in the weak-link, more complicated dynamics interacting with surfaces and narrowed structures are quite possible. At this point, this problem needs more theoretical investigations.

In conclusion, we have fabricated triplet p-wave superconducting weak-link and observed the second harmonic components in the current response to the applied magnetic field. With in-plane magnetic field present, the second harmonic term emerges and grows when the field is increased.

Chapter 7

Conclusions

Sr_2RuO_4 is believed to be a spin-triplet superconductor whose order parameter is described by $\mathbf{d} = \mathbf{z}(p_x \pm ip_y)$. If those are confirmed, Sr_2RuO_4 will be the one of the most fascinating examples to demonstrate fundamental physics of unconventional superconductivity as well as to have far-reaching implications on quantum computing applications. However, since the discovery in 1994, there still are more questions than answers about its superconducting properties.

To test the core theoretical predictions on the superconductor, we performed cantilever torque magnetometry experiments on chiral domains, half-quantized fluxoids, and weak-link junctions in Sr_2RuO_4. The purity of the crystal was very important factor in the experiment, and much attention paid to maintain the quality of the sample throughout the sample preparation to actual measurements. All samples were crushed by hand, and fabricated one by one with the focused ion beam, so there is unavoidable randomness in each sample. In analyzing data we tried to focus on the consistent trends among those different samples, and paid extra caution to rule out any peculiarity caused by the sample geometry or the defects.

With the measurements of magnetic response from the chiral order parameter domains, we conclude that, in our measurement resolution, any magnetic signal from the domain currents are several orders of magnitude lower than theoretically predicted. This confirms the experiments by Kirtley et al. [20]. It is tempted to argue that the order parameter might not break time-reversal symmetry. However, given the convincing evidence from Josephson interferometry, μSR, and Kerr rotation measurements, it is more reasonable to investigate the theatrical predictions/speculations about the mechanisms which still maintain the time-reversal symmetry broken states, and only decrease the chiral current strength.

The central finding of the course of investigations is the evidence that half-quantized fluxiod states are stabilized in a mesoscopic (~1 μm) sample of Sr_2RuO_4. We found that in-plane magnetic fields favor the appearance of the half-quantized states, and the stability region grows linearly with the field. We propose the kinematic spin polarization mechanism that is consistent with spin-triplet equal-spin-paring states. It should be noted that the existence of half-quantized vortices doesn't mandate the $p_x \pm ip_y$ order parameter. A striking consequence of the half-quantized vortex in a spin-triplet superconductor is the presence of the spin current associated with $\mathbf{d}$-vector rotation. To investigate the charge and spin dynamics, we fabricated weak-link junctions embedded in Sr_2RuO_4 rings, and observed unusual current-phase relationships. Our model based on Gibbs free energy with the Josephson coupling of two independent spin species successfully fit the data, and thus suggests that the spin current is a possible explanation for the abnormal current phase relationship.

Sr_2RuO_4 is the superconductor quite hard to grow, fabricate and perform measurements on, as well as its unimpressive low transition temperature. However, it is easily counterweighted by the fact that it shows fascinating physics inherited from superfluid ^{3}He, and is possibly harboring exotic Majorana fermions in the core of the half-quantized vortices, which is proposed to shows non-Abelian statistics and to be used as topological qubits. We believe that our research contributed to more understanding of the physics in this material and stimulated future researches to come.

.

References

[1] V.L. Ginsburg and L.D. Landau, Zh. Eksp. Teor. Fiz 1950 (1950).

[2] J. Bardeen, L.N. Cooper, and J.R. Schrieffer, Physical Review **108**, 1175 (1957).

[3] L.P. Gorkov, Sov. Phys. JETP **9**, 1364–1367 (1959).

[4] Y. Maeno, H. Hashimoto, K. Yoshida, S. Nishizaki, T. Fujita, J. G. Bednorz, and F. Lichtenberg, Nature **372**, 532-534 (1994).

[5] A. P. Mackenzie and Y. Maeno, Reviews of Modern Physics **75**, 657 (2003).

[6] A. P. Mackenzie, N. E. Hussey, A. J. Diver, S. R. Julian, Y. Maeno, S. Nishizaki, and T. Fujita, Physical Review. B, Condensed Matter **54**, 7425-7429 (1996).

[7] T. Oguchi, Physical Review B **51**, 1385-1388 (1995).

[8] C. Bergemann, A. P. Mackenzie, S. R. Julian, D. Forsythe, and E. Ohmichi, Advances in Physics **52**, 639-725 (2003).

[9] T. Imai, a. Hunt, K. Thurber, and F. Chou, Physical Review Letters **81**, 3006-3009 (1998).

[10] Y. Sidis, M. Braden, P. Bourges, B. Hennion, S. NishiZaki, Y. Maeno, and Y. Mori, Physical Review Letters **83**, 3320-3323 (1999).

[11] S. NishiZaki, Yoshiteru Maeno, and Zhiqiang Mao, Journal of Low Temperature Physics **117**, 1581–1585 (1999).

[12] P. W. Anderson, Science **256**, 1526-1531 (1992).

[13] A. P. Mackenzie, R. K. W. Haselwimmer, A. W. Tyler, G. G. Lonzarich, Y. Mori, S. Nishizaki, and Y. Maeno, Physical Review Letters **80**, 161 (1998).

[14] Z. Q. Mao and Y. Mori, Physical Review B **60**, 610-614 (1999).

[15] T. Akima, S. NishiZaki, and Y. Maeno, Journal of the Physical Society Of **68**, 694 (1999).

[16] M. Sigrist and K. Ueda, Reviews of Modern Physics **63**, 239 (1991).

[17] J. F. Annett, Advances in Physics **39**, 83 (1990).

[18] G. M. Luke, Y. Fudamoto, K. M. Kojima, and M. I. Larkin, Nature **394**, 558-561 (1998).

[19] J. Xia, Y. Maeno, P. T. Beyersdorf, M. M. Fejer, and A. Kapitulnik, Physical Review Letters **97**, 167002-4 (2006).

[20] J. R. Kirtley, C. Kallin, C. W. Hicks, E.-A. Kim, Y. Liu, K. A. Moler, Y. Maeno, and K. D. Nelson, Physical Review B (Condensed Matter and Materials Physics) **76**, 014526-8 (2007).

[21] K. Ishida, H. Mukuda, Y. Kitaoka, K. Asayama, Z. Q. Mao, Y. Mori, and Y. Maeno, Nature **396**, 658-660 (1998).

[22] K. Ishida, H. Mukuda, Y. Kitaoka, Z. Mao, H. Fukazawa, and Y. Maeno, Physical Review B **63**, 4-7 (2001).
[23] J. A. Duffy, S. M. Hayden, Y. Maeno, Z. Mao, J. Kulda, and G. J. McIntyre, Physical Review Letters **85**, 5412 (2000).
[24] T. M. Rice, M. Sigrist, and Y. Maeno, New Journal of Physics **11**, 055052 (2009).
[25] T. M. Riseman, P. G. Kealey, E. M. Forgan, A. P. Mackenzie, L. M. Galvin, A. W. Tyler, S. L. Lee, C. Ager, D. McK. Paul, C. M. Aegerter, R. Cubitt, Z. Q. Mao, T. Akima, and Y. Maeno, Nature **396**, 242-245 (1998).
[26] G. E. Volovik, Sov. Phys. JETP **61**, 843 (1985).
[27] G. E. Volovik, JETP Lett **39**, (1984).
[28] M. Stone and R. Roy, Physical Review B **69**, 1-12 (2004).
[29] C. Kallin and A. J. Berlinsky, Journal of Physics. Condensed Matter : an Institute of Physics Journal **21**, 164210 (2009).
[30] M. Sigrist, T. M. Rice, and K. Ueda, Physical Review Letters **63**, 1727–1730 (1989).
[31] M. Matusumoto and M. Sigrist, Journal of the Physical Society of Japan **68**, 994-1007 (1999).
[32] A. Amann, Ana Mota, M. Maple, and H. V. Löhneysen, Physical Review B **57**, 3640-3649 (1998).
[33] A. C. Mota, E. Dumont, and J. L Smith, Physical Review B **117**, 1477-1481 (1999).
[34] A. C. Mota, E. Dumont, A. Amann, and Y. Maeno, Physica B: Condensed Matter **259**, 934–935 (1999).
[35] M. Sigrist and D. F. Agterberg, Progress of Theoretical Physics **102**, 965-981 (1999).
[36] V. O. Dolocan, C. Veauvy, F. Servant, P. Lejay, K. Hasselbach, Y. Liu, and D. Mailly, Physical Review Letters **95**, 097004-4 (2005).
[37] G. E. Volovik and V.P. Mineev, JETP Lett **24**, 561 (1976).
[38] M. C. Cross and W. F. Brinkman, Journal of Low Temperature Physics **27**, 683-686 (1977).
[39] N. B. Kopnin and M. M. Salomaa, Physical Review B **44**, 9667 (1991).
[40] N. Read and D. Green, Physical Review B **61**, 10267-10297 (2000).
[41] A.Yu. Kitaev, Annals of Physics **303**, 2-30 (2003).
[42] S. B. Chung, H. Bluhm, and E.-A. Kim, Physical Review Letters **99**, 197002-4 (2007).
[43] Z. Q. Mao, Y. Maeno, and H. Fukazawa, Materials Research Bulletin **35**, 1813-1824 (2000).
[44] D. Rugar, H. J. J. Mamin, and P. Guethner, Applied Physics Letters **55**, 2588–2590 (1989).
[45] T. Fukuma, M. Kimura, K. Kobayashi, K. Matsushige, and H. Yamada, Review of Scientific Instruments **76**, 053704 (2005).
[46] E.R.I. Abraham and E.A. Cornell, Applied Optics **37**, 1762–1763 (1998).
[47] J. Jang, R. Budakian, and Y. Maeno, Applied Physics Letters **98**, 132510 (2011).
[48] G. Binnig, C.F. Quate, and C. Gerber, Physical Review Letters **56**, 930–933 (1986).

[49] D. Rugar, R. Budakian, H. J. Mamin, and B. W. Chui, Nature **430**, 329-32 (2004).
[50] R. Budakian, H. J. Mamin, B. W. Chui, and D. Rugar, Science (New York, N.Y.) **307**, 408-11 (2005).
[51] T. R. TR Albrecht, P. Grutter, D. Horne, and D. Rugar, Journal of Applied **69**, 668-673 (1991).
[52] J. A. Sidles, J. L. Garbini, K. J. Bruland, D. Rugar, O. Züger, S. Hoen, and C. S. Yannoni, Reviews of Modern Physics **67**, 249 (1995).
[53] F. Kidwingira, J. D. Strand, D. J. Van Harlingen, and Y. Maeno, Science **314**, 1267-1271 (2006).
[54] K. D. Nelson, Z. Q. Mao, Y. Maeno, and Y. Liu, Science **306**, 1151-1154 (2004).
[55] P. Ashby and C. Kallin, Physical Review B **79**, 1-6 (2009).
[56] T. A. Tokuyasu, D. W. Hess, and J. A. Sauls, Physical Review B **41**, (1990).
[57] S. Raghu, A. Kapitulnik, and S. Kivelson, Physical Review Letters **105**, (2010).
[58] D. F. Agterberg and T. M. Rice, Physical Review Letters **78**, 3374-3377 (1997).
[59] A. J. Leggett, in *Quantum Liquids: "Bose Condensation and Cooper Pairing in Condensed-Matter Systems"* (2006).
[60] J. Jang, D. G. Ferguson, V. Vakaryuk, R. Budakian, S. B. Chung, P. M. Goldbart, and Y. Maeno, Science **331**, 186-188 (2011).
[61] H. Murakawa, K. Ishida, K. Kitagawa, Z. Q. Mao, and Y. Maeno, Physical Review Letters **93**, 167004 (2004).
[62] B. J. Baelus, F. M. Peeters, and V. A. Schweigert, Physical Review B **61**, 9734 (2000).
[63] D. Y. Vodolazov, B. J. Baelus, and F. M. Peeters, Physical Review B **66**, 054531 (2002).
[64] V. Vakaryuk and A. J. Leggett, Physical Review Letters **103**, 057003-4 (2009).
[65] A. J. Leggett, Reviews of Modern Physics **47**, 331-414 (1975).
[66] Y. Yoshioka and K. Miyake, Journal of the Physical Society of Japan **78**, 074701 (2009).
[67] Y. Maeno, K. Yoshida, H. Hashimoto, S. Nishizaki, S. Ikeda, M. Nohara, T. Fujita, A. P. Mackenzie, N. E. Hussey, J. G. Bednorz, and F. Lichtenberg, Journal of the Physics Society Japan **66**, 1405-1408 (1997).
[68] J. R. Kirtley, C. C. Tsuei, M. Rupp, J. Z. Sun, L. S. Yu-Jahnes, A. Gupta, M. B. Ketchen, K. A. Moler, and M. Bhushan, Physical Review Letters **76**, 1336 (1996).
[69] N. Yoshida, Y. Tanaka, J. Inoue, and S. Kashiwaya, Journal of the Physics Society Japan **68**, 1071-1074 (1999).
[70] H. Suderow, V. Crespo, I. Guillamon, S. Vieira, F. Servant, P. Lejay, J. P. Brison, and J. Flouquet, New Journal of Physics **11**, 093004 (2009).
[71] D. A. Ivanov, Physical Review Letters **86**, 268-271 (2001).
[72] G. Moore and N. Read, Nuclear Physics B **360**, 362–396 (1991).
[73] A. Kitaev, Annals of Physics **321**, 2-111 (2006).
[74] J. Sau, R. Lutchyn, S. Tewari, and S. Das Sarma, Physical Review B **82**, 1-7 (2010).

[75] K. Likharev, Reviews of Modern Physics **51**, 101-159 (1979).
[76] A. H. Silver and J. E. Zimmerman, Physical Review **157**, 317 (1967).
[77] G. Rashedi, Y. Rahnavard, and Y.A. Kolesnichenko, Low Temperature Physics **36**, 205 (2010).
[78] S. Backhaus, S. Pereverzev, R. W. Simmonds, A. Loshak, J. C. Davis, and R. E. Packard, **392**, 687-690 (1998).
[79] A. Marchenkov, R. Simmonds, S. Backhaus, A. Loshak, J. Davis, and R. Packard, Physical Review Letters **83**, 3860-3863 (1999).
[80] J. Viljas and E. Thuneberg, Physical Review Letters **83**, 3868-3871 (1999).
[81] S.-K. Yip, Physical Review Letters **83**, 3864-3867 (1999).